Supplementary Information

# Reaction-driven ionic remodeling enables durable soft electronics

Ji Hong Kim[1]†, Yeongjun Yoon[1]†, Sung Gyu Shin[2]†, Won Hyuk Choi[1], Jong Hwi Kim[1], Yoseph Park[1], Joo Sung Kim[5], Hanbin Choi[6], Hyo Jeong Kim[7], So Young Kim[1], Youngho Eom[7], Jae Hyun Jeong[2*], Kyeounghak Kim[1*], and Do Hwan Kim[1,3,4*]

[1]*Department of Chemical Engineering, Hanyang University, Seoul 04763, Republic of Korea.*
[2]*Department of Chemical Engineering, Soongsil University, Seoul, 06978, Republic of Korea.*
[3]*Institute of Nano Science and Technology, Hanyang University, Seoul 04763, Republic of Korea.*
[4]*Clean-Energy Research Institute, Hanyang University, Seoul 04763, Republic of Korea.*
[5]*Thin-Film Device Laboratory, RIKEN, 2-1 Hirosawa, Wako, Saitama 351-0198, Japan.*
[6]*Department of Chemical and Biomolecular Engineering, North Carolina State University, Raleigh, NC, USA*
[7]*Department of Organic and Nano Engineering, Human-Tech Convergence Program, Hanyang University, Seoul, 04763, Republic of Korea*

†These authors contributed equally to this work.

*Corresponding authors' email: nfejjh@ssu.ac.kr (J.H.J.), chemekim@hanyang.ac.kr (K.K.), dhkim76@hanyang.ac.kr (D.H.K.)

# Table of contents

**Supplementary Methods**


| | |
|---|---|
| Material characterization | 3 |
| Mechanical property | 3 |
| Electrical characterization | 4 |
| Gas Chromatograph | 5 |
| Dynamic Vapor Sorption (DVS) | 5 |
| Nuclear Magnetic Resonance (NMR) Spectroscopy | 6 |
| Computational Details | 6 |
| Engineered skin organoid–based wound healing model | 8 |


**Supplementary Note**


| | |
|---|---|
| Ionic conductivity of ion-conducting gel | 11 |
| Ionicity of ion-conducting gel | 12 |


**Supplementary Figure**


| | |
|---|---|
| Supplementary Figure 1. Schematic illustration comparing hydrogel, ion gel, and gelatin based REACT gel | 14 |
| Supplementary Figure 2. Molecular structures of the constituent materials for the REACT gel | 15 |
| Supplementary Figure 3. Water-content-dependent ionic conductivity of choline malate, choline glycolate and choline propionate ionic liquids | 16 |
| Supplementary Fig. 4. PFG-NMR analysis of choline and malate ion diffusivity in pure CM, hydrated CM and gelatin-based REACT gel | 17 |
| Supplementary Figure 5. PFG-NMR-derived ion diffusivity in REACT gels with different ionic liquid contents | 18 |
| Supplementary Figure 6. Gel-assisted amplification of free-ion population in REACT gels with increasing ionic liquid content | 19 |
| Supplementary Figure 7. Representative molecular configurations and simulation cells used for on-the-fly MLFF training of choline malate ionic liquid, hydrated ionic liquid, and collagen-containing electrolyte systems | 20 |
| Supplementary Figure 8. Parity plots demonstrating the alignment between DFT and MLIP predictions for energies and atomic forces in the hydrated choline malate ionic liquid model | 21 |
| Supplementary Figure 9. Representative MLIP simulation cells constructed to examine the effects of hydration and collagen incorporation on ion dissociation and transport in choline malate ionic liquid systems | 22 |
| Supplementary Fig. 10. Temporal profiles of temperature and total energy confirming stable NVT dynamics for the pure, hydrated, and collagen-containing choline malate ionic liquid systems | 23 |
| Supplementary Fig. 11. Schematic illustration of radial distribution functions (RDFs) for $[Ma]^{2-}$-$H_2O$ and [Ch]-[MA] pairs | 24 |
| Supplementary Fig. 12. Generality of amino-acid-assisted ion decarboxylation in chitosan ion gels | 25 |
| Supplementary Fig. 13. XPS analysis of REACT gels with different ionic liquid contents | 26 |

| | |
|---|---|
| Supplementary Fig. 14. FT-IR analysis of REACT gels with different ionic liquid contents | 27 |
| Supplementary Fig. 15. Distance-dependent mobility analysis showing that [Ch]+ ions located closer to collagen oxygen atoms exhibit suppressed diffusion, indicating interfacial confinement by the collagen matrix | 28 |
| Supplementary Fig. 16. Local configurations of [Ch]+ ions confined within interstitial collagen environments, highlighting their potential role as electrostatic bridges between neighboring collagen molecules | 29 |
| Supplementary Fig. 17. Mobility–distance correlation analysis showing that [Ma]2− functional groups exhibit no clear interstitial confinement with collagen, unlike the localized anchoring behavior observed for [Ch]+ ions. | 30 |
| Supplementary Fig. 18. Mechanical properties of REACT gels with different ionic liquid contents | 31 |
| Supplementary Fig. 19. Rheological analysis of internal interactions and viscoelastic properties of REACT gels | 32 |
| Supplementary Fig. 20. DSC analysis of REACT gels with different ionic liquid contents | 33 |
| Supplementary Fig. 21. Water activity of PEO-based hydrogel and REACT gel | 34 |
| Supplementary Fig. 22. TGA analysis of water retention in REACT gels with different ionic liquid contents | 35 |
| Supplementary Fig. 23. SEM images of REACT gels with different ionic liquid contents | 36 |
| Supplementary Fig. 24. Electrochemical performance of chitosan ion gel and REACT gel | 37 |
| Supplementary Fig. 25. Current-density output of the REACT gel under DC pulsing | 38 |
| Supplementary Fig. 26. Ion-leakage behavior of conventional hydrogel and REACT gel in PBS | 39 |
| Supplementary Fig. 27. Long-term electrical sustainability of the REACT gel during PBS soaking | 40 |
| Supplementary Fig. 28. Electrochemical stability of the REACT gel | 41 |
| Supplementary Fig. 29. Cytocompatibility assessment of ionic gels | 42 |
| Supplementary Fig. 30. Differentiation and assembly of engineered skin organoids | 43 |
| Supplementary Fig. 31. Structural maturation and barrier formation of engineered skin organoids monitored by TEER measurements | 44 |
| Supplementary Fig. 32. Wound healing dynamics in biopsy punch–injured E-skin organoids under different gel treatments | 45 |
| Supplementary Fig. 33. OCT-based visualization of epidermal regeneration in laser-induced wounds of E-skin organoids | 46 |
| Supplementary Fig. 34. Enhanced angiogenic activity induced by ionic gel during HUVEC tubular formation | 47 |


**Supplementary Note**


| | |
|---|---|
| Table S1. | 48 |
| Table S2. | 49 |
| Table S3. | 50 |

**Supplementary References** 51


**Other Supplementary Information for this manuscript includes the following:**

Supplementary video

## Supplementary Methods

### Material characterization

UV-vis-NIR spectroscopy (Jasco, V-770) was employed to measure the optical absorbance of the Au nanoparticles. Infrared spectra were acquired on a Bruker Optics GmbH (Germany) spectrometer configured in attenuated total reflection (ATR) mode with a ZnSe crystal. For each measurement, 256 scans were co-added at a resolution of 1 $cm^{-1}$ across the 4000 to 450 $cm^{-1}$ window. Deconvolution of the FTIR bands was performed by iterative Gaussian peak fitting until an optimal fit was reached. Surface morphology of the Au nanoparticle films was examined by field-emission scanning electron microscopy (FE-SEM, JSM-6700F, JEOL), with elemental composition assessed through an attached EDS detector. Raman measurements were carried out on a Thermo Scientific™ DXR™2 Raman microscope coupled with the DXR™2xi Raman imaging system. Raman imaging used a 532 nm excitation laser at 2.0 mW, yielding a spot size of roughly 10 $\mu m^2$ and a spatial resolution of 3 μm. Zeta potential was determined on a Malvern Zetasizer NanoZS operating in backscatter mode under an applied working voltage of 40 V. The interaction of gelatin and CM was subjected to characterization through X-ray photoelectron spectroscopy (Thermo Fisher Scientific, XPS-Theta Probe). The binding energy of each sample was calculated by the AES & XPS program.

### Mechanical property

A universal testing machine (UTM QRUTS-S105, QURO) equipped with a 1-kN load cell was used to evaluate the mechanical properties of all polymer films at 25°C, applying a stretching speed of 10 mm/min. The samples were prepared and tested following ASTM standards (Test Method D 638-02a, specimen type V). Young's modulus (Y) was determined from the slope of the stress-strain curves within the 0–5% strain range. The mechanical properties reported in this study are expressed as the mean ± standard deviation, based on five samples tested under

identical experimental conditions.

Thermogravimetric analysis (TGA) and Differential Scanning Calorimetry (DSC) were conducted using an SDT-Q600 instrument from TA Instruments to confirm the water content and phase transition in REACT gel under a nitrogen ($N_2$) atmosphere. The analysis was performed in a temperature range from 20 ℃ to 820 ℃ and 25 ℃ to 300 ℃ with a ramp rate of 10 ℃/min, utilizing a sample weight of 5 mg.

Rheological characterization was carried out using an oscillatory rheometer (MCR302e, Anton Paar, Austria) configured with a 25 mm parallel-plate geometry. For each measurement, film specimens roughly 0.5 mm in thickness were loaded between the plates. Frequency sweeps were further performed across an angular frequency range from 0.05 to 500 rad $s^{-1}$ while holding the shear strain constant at 1%.

**Electrical characterization**

Electrochemical impedance spectroscopy (EIS) is an essential method for investigating ion transport phenomena within polymer electrolytes and their interfaces, such as electrode–electrolyte interactions. EIS measurements were carried out at room temperature using a PGSTAT302N electrochemical analyzer (Metrohm Autolab) over a frequency range of 0.1 Hz to 100 kHz with a 10 mV AC signal. A coin cell assembly from Hohsen Corp. (Japan) was utilized to conduct EIS tests on various polymer films under different conditions, including with and without applied pressure. In these measurements, polymer films with a thickness of approximately 500 μm were positioned between two stainless steel discs (10 mm in diameter, serving as electrodes) to create a piezocapacitive device configuration. The impedance spectra were analyzed and fitted with appropriate equivalent circuit models using NOVA software (Metrohm Autolab) to determine the bulk resistance (Rb) of the devices. Ionic conductivity (σ) was calculated from the bulk resistance according to the equation:

$$\sigma = \left(\frac{l}{R_b \times A}\right)$$

where $\sigma$ is the ionic conductivity, $l$ is the thickness of the polymer film between the electrodes, $A$ is the electrode area, and $R_b$ is the bulk resistance derived from the Nyquist plots. Capacitance measurements were performed at room temperature using an Agilent E4980A Precision LCR Meter.

**Gas Chromatograph**

After initiating the reaction, the system was monitored continuously for more than 30 min. Product analysis was performed on a gas chromatograph (YL6500 GC, Korea) fitted with a flame ionization detector (FID), an autosampler (YL6500 GC, Korea), and a DB-624 UI column (60 m × 0.32 mm × 1.80 μm, Agilent, USA). The column oven was held isothermally at room temperature throughout all measurements.

**Dynamic Vapor Sorption**

The moisture sorption behavior of the gelatin-based samples was characterized by dynamic vapor sorption (DVS) using deionized water as the solvent. Measurements were performed at a constant temperature of 25 °C under a total carrier gas flow of 200 sccm, with the desired relative humidity (RH) generated by mixing dry and water-saturated gas streams. Approximately 5 to 6 mg of each sample was loaded onto the microbalance and first equilibrated at 0% RH to establish a dry reference mass. The RH was then increased stepwise from 0% to 90% in 10% increments during the sorption branch, after which it was decreased from 90% back to 0% in the same 10% steps during the desorption branch, completing one full sorption-desorption cycle. At each RH step, the humidity was held constant until the sample mass reached equilibrium, defined by a change in mass per unit time (dm/dt) falling below a

preset threshold, before advancing to the next step. The equilibrium mass uptake at each RH was used to construct the sorption and desorption isotherms.

**Nuclear Magnetic Resonance (NMR) Spectroscopy**

Ion and water diffusivities in the PEO-based hydrogel and the choline malate containing ion-conducting gel were measured by PFG-NMR diffusometry on a Bruker Avance III HD 500 MHz (11.7 T) spectrometer equipped with a Diff30 PFG diffusion probe (National Center for Inter-University Research Facilities, Seoul National University), using deionized water as the solvent. The PFG spin-echo sequence employed a 9.8 μs 90° radio frequency (RF) pulse, a gradient pulse duration (δ) of 1.0 ms, a diffusion time (Δ) of 50.0 ms, and a gradient strength of 100%. A single 90° RF pulse of 9.8 μs at 29 W was applied, and $^{1}$H NMR spectra were acquired with an acquisition time of 1.0922667 s, a pre-scan delay of 6.5 μs, and a relaxation delay of 4.0 s. For each condition, 16 scans were co-added. Measurements were carried out over five temperature steps from 298 to 318 K at 5 K intervals, and the self-diffusion coefficients were extracted by fitting the signal attenuation to the Stejskal-Tanner equation. Transverse relaxation times ($T_2$) were measured using the Carr-Purcell-Meiboom-Gill (CPMG) pulse sequence, with the echo train recorded over a series of inter-pulse spacings, and $T_2$ was obtained by fitting the decay of the echo amplitude to a single exponential function. All measurements were carried out at 298K under temperature control.

**Computational Details**

To develop a machine learning interatomic potential (MLIP) for a system comprising an ionic liquid (choline $[Ch]^+$ and malate $[Ma]^{2-}$), water ($H_2O$), and gelatin, we first performed density functional theory (DFT) calculations using QM/MM simulation cluster (NFEC-2025-02-303332) and the Vienna Ab-initio Simulation Package (VASP, version 6.4.3)[1-2]. To accurately describe the potential energy surface, we employed the projector augmented wave

(PAW) method and the revPBE-D3 exchange-correlation functional within the GGA framework[3-5], which is well-regarded for its high accuracy in describing aqueous and ionic liquid systems[6-9]. A plane-wave cutoff energy of 450 eV was applied. The convergence criteria for electronic energy and ionic forces were set to $10^{-5}$ eV and 0.01 eV/Å, respectively.

To efficiently sample the ab-initio frames for training the MLIP, we adopted the on-the-fly machine learning force field (MLFF) method available in VASP software, which is based on the Gaussian approximation potential (GAP). The computational models for the on-the-fly MLFF simulations are depicted in Supplementary Fig. 6 (the initial structure of the collagen molecule was referenced from the Protein Data Bank, PDB ID: 1CGD)[10]. Based on these models, NPT simulations were conducted at 300 K, generating 670, 545, and 1632 ab-initio frames for the pure ionic liquid ($12[Ch]^+ + 6[Ma]^{2-}$), ionic liquid with 50 wt% $H_2O$ ($8[Ch]^+ + 4[Ma]^{2-} + 76H_2O$), and ionic liquid with water and collagen ($2[Ch]^+ + 1[Ma]^{2-} + 16H_2O$ + 1 Collagen), respectively.

Then, the obtained ab-initio frames were randomly split into training and validation datasets with an 85:15 ratio. The MLIP was then developed using the SevenNet package[11], with FlashTP[12] acceleration. The resulting MLIP showed mean absolute errors (MAEs) of 1.581 meV/atom for energy and 40.28 meV/Å for forces on the validation dataset. To assess the generalization capability of our MLIP on out-of-domain data, we performed a 10 ns classical molecular dynamics simulation (1 fs timestep) of the ionic liquid with 50 wt% $H_2O$ model (Supplementary Fig. 6f) at 300 K using the COMPASS III force field in the Materials Studio program[13-14]. From this trajectory, 30 frames were extracted at uniform intervals. Single-point DFT and MLIP calculations were performed on these frames, and the resulting energies and forces were compared in a parity plot (Supplementary Fig. 7). The results confirmed that our MLIP exhibits sufficient robustness for out-of-domain configurations. Developed MLIP

potential and datasets are available at:

https://github.com/evenfarther/choline_malate_h2o_collagen.

For production of simulations, four distinct systems were constructed: (i) a pure ionic liquid model comprising 40$[Ch]^{+}$ and 20$[Ma]^{2-}$ (Supplementary Fig. 8a); (ii) a hydrated model with 18$[Ch]^{+}$, 9$[Ma]^{2-}$, and 170 $H_2O$ molecules, corresponding to a 50 wt% water concentration (Supplementary Fig. 8b); (iii) a single-collagen system containing 38$[Ch]^{+}$, 19$[Ma]^{2-}$, 302 $H_2O$, and 1 collagen molecule, which mimics the experimental ionic liquid-to-water ratio in the presence of collagen (Supplementary Fig. 8c); and (iv) a double-collagen system with the same solvent composition but containing two collagen molecules (Supplementary Fig. 8d). Using the trained MLIP, NVT simulations were performed for 2 ns for each system. The convergence of total energy and temperature throughout the simulations confirmed that all systems reached equilibrium (Supplementary Fig. 9).

All MD simulations were carried out using the Large-scale Atomic/Molecular Massively Parallel Simulator (LAMMPS) code[15]. Post-processing analyses, including the calculation of radial distribution functions (RDFs) and diffusion coefficients, were performed using the MDAnalysis Python library[16-17]. Visualization of the simulation trajectories and diffusion paths was conducted using OVITO software[18].

**Engineered skin organoid-based wound healing model**

To quantitatively evaluate the wound-healing efficacy of the ionic gel under electrochemical stimulation, we established a highly reproducible engineered skin organoid (E-skin organoid) platform derived from human induced pluripotent stem cells (hiPSCs). A detailed illustration is provided in Supplementary Fig. 29. hiPSCs (ATCC) were cultured on dishes coated with 1.0% Matrigel in serum-free medium (SFM) supplemented with the ROCK

inhibitor Y-27632(10 μM) to maintain colony formation. Colonies were dissociated into single cells using Accutase and filtered through a 35 μm cell strainer. The cells were subsequently seeded into U-bottom low-attachment 96-well plates at a density of 35,000 cells/ml to induce spheroid formation. To guide epidermal lineage differentiation, spheroids were cultured in an E6-based differentiation medium containing 2.0% Matrigel, SB-431542 (10 μM), bFGF (4 ng/ml), and BMP4 (5 ng/ml). After 3 days of culture, LDN-193189 (1.0 μM) and bFGF (250 ng/ml) were added to modulate BMP signaling, enabling the generation of skin-like organoids that recapitulate key cellular components of human skin.

A dermal equivalent was prepared by mixing human dermal fibroblasts (HDFn, 10,000 cells/ml) with chilled collagen solution (Advanced Biomatrix, 400 μl) supplemented with buffering reagents ($NaHCO_3$ 0.26 M, HEPES 0.2 M and NaOH 0.04 N). The mixture was polymerized in 12-well inserts for 1 h to form a fibroblast-embedded dermal matrix. The differentiated skin organoids were then combined with human epidermal keratinocytes (HEKn) at a 1:1 ratio to generate a cell cocktail (80,000 cells), which was seeded onto the dermal matrix. Epidermal stratification was subsequently induced through air–liquid interface (ALI) culture for 7 days.

Wound models were generated in the mature E-skin organoids by either creating a tissue defect using a 3-mm biopsy punch or inducing micro-damage using a $CO_2$ laser (1 W, 10 ms, 200 μm). Ionic gel (IL 80%) or control hydrogel was applied to the wound region. Electrical pulse stimulation (1 kHz, 500 mVpp, -250 mV offset, 50% duty cycle) was delivered using a function generator while organoids were maintained at 37 °C to monitor wound-healing dynamics. Wound closure and epidermal regeneration were visualized using optical microscopy, stereoscopy, and optical coherence tomography (OCT), and the extent of wound repair was quantified using Image*J* analysis. The structural integrity and maturation of the E-

skin organoids were continuously monitored by transepithelial electrical resistance (TEER) measurements using an EVOM3 epithelial volt-ohm meter. Cytocompatibility of the ionic gel was evaluated by MTT assays using HDFn and HEKn cultured in Transwell systems. In addition, biochemical analyses of the culture medium were performed to quantify pro-collagen production and vascular endothelial growth factor (VEGF) secretion during wound regeneration. The biological activity of secreted growth factors was further assessed using a HUVEC tubular formation assay on Matrigel-coated plates. Quantitative analysis of angiogenic structures, including junctions, segments and meshes, was conducted using the ImageJ Angiogenesis Analyzer. Statistical significance was determined using one-way ANOVA followed by Tukey's multiple comparison test.

## Supplementary Note

**Ionic conductivity of ion-conducting gel**

The theoretical ionic conductivity of ion-conducting gels is typically calculated using the Nernst-Einstein (NE) equation (1) :

$$\sigma_{NE} = \frac{N_C q^2 D}{kT} \quad (1)$$

where $\sigma_{NE}$ is ionic conductivity, $N_C$ is ion number density, $q$ is ion charge, $D$ is ion diffusivity, $k_B$ is Boltzmann constant, and $T$ is temperature. However, measured conductivity deviates substantially from theoretical value using NE equation. This deviation primarily originates from the assumptions of the NE equation, which implicitly treats all introduced charge carriers as fully dissociated and independently mobile, while neglecting ion–ion correlations, specific interactions, and hopping-mediated transport. In practical systems, particularly in ionic liquids, ions exist partially as clusters rather than fully free species. This reduces the number of mobile charge carriers below the initial input concentration and lowers diffusivity due to the large cluster volume. To account for these real-system deviations, the Haven ratio ($H_R$) was developed[19-21], defined as the ratio of measured to theoretical ionic conductivity, and serves here as a quantitative measure of ionicity across gel systems.

$$H_R = \frac{\sigma_{NE}}{\sigma_{Measured}} = \frac{\frac{N_C q^2 D}{kT}}{\sigma_{exp}} \quad (2)$$

$$\frac{1}{H_R} = k\,(ionicity) = \frac{\sigma_{Measured}}{\sigma_{NE}} = \frac{[free\ ions]}{[total\ ions]} \quad (3)$$

According to this relationship, once the effective ion diffusivity is experimentally determined, the ionicity can be quantitatively evaluated even in the solid state, enabling an assessment of how readily clustered ions dissociate within the gel. We determined the number of free ions and the resulting ionicity using the corresponding relationship. Although these

calculated values may deviate from the absolute physical quantities, they remain entirely valid for a comparative analysis of the relative trends across different material groups.

**Ionicity of ion-conducting gel**

The ionicity of an ionic liquid (IL) gel is defined as the fraction of ions that are fully dissociated and independently mobile, relative to the total number of ions introduced into the system. Ionicity less than unity arises because ions in real systems do not exist exclusively as free species; a significant fraction associates into neutral or low-mobility ion pairs and clusters, which do not contribute to conductivity. This note describes a complete, step-by-step procedure for quantifying ionicity in gels incorporating the choline-malate ionic liquid, using experimentally accessible quantities: the measured ionic conductivity ($\sigma_{meas}$) and the self-diffusion coefficients of individual ionic species ($D_i$) obtained from pulsed-field-gradient nuclear magnetic resonance (PFG-NMR) and electrochemical impedance spectroscopy (EIS) analysis.

Choline-malate consists of two ionic species:

Choline cation ($Ch^+$): monovalent, charge number $|z_{Ch}| = 1$

Malate anion ($Ma^{2-}$): divalent, charge number $|z_{Ma}| = 2$

Charge neutrality requires that for every malate anion there are two choline cations. If the total number density of ion pairs (formula units) is $N_0$ (units: $m^{-3}$), then the individual number densities are:

$$N_{Ch} = 2N_0, \qquad N_{Ma} = N_0$$

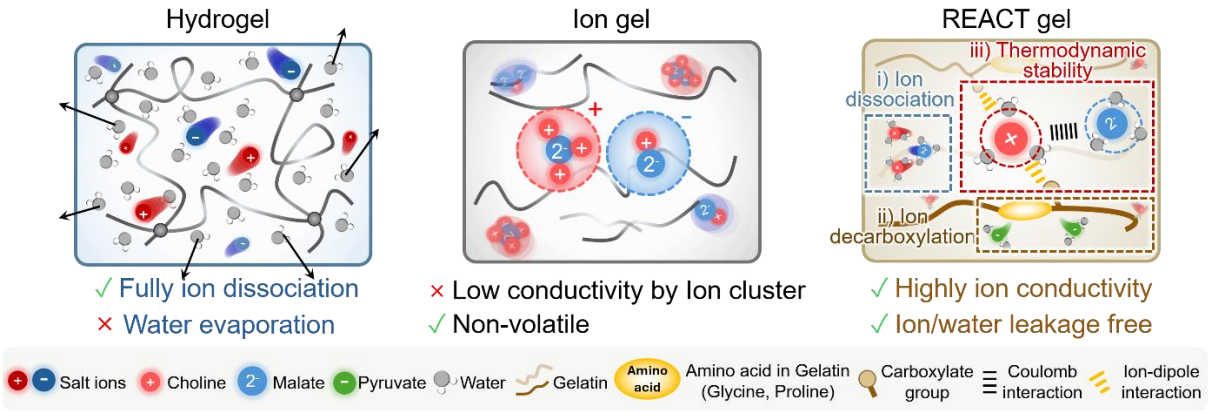
In practice, $N_0$ is calculated from the molar concentration $c_0$ (mol $m^{-3}$) of the ionic liquid as:

$$N_0 = c_0 \times N_A$$

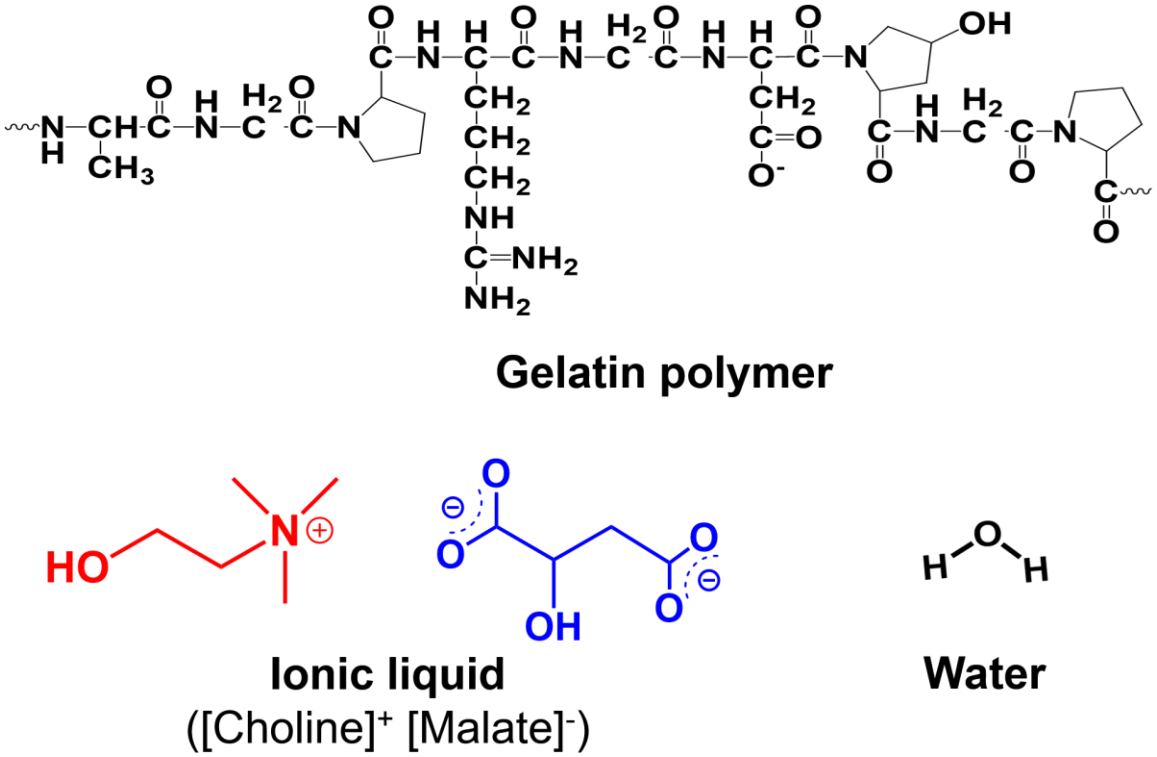
where $N_A = 6.022 \times 10^{23}$ $mol^{-1}$ is Avogadro's number.

Once the experimental inputs are obtained, the ionicity follows directly by substitution. The measured conductivity $\sigma_{meas}$ is taken from EIS, and the self-diffusion coefficients $D_{Ch}$ and $D_{Ma}$ are taken from PFG-NMR, all at the same temperature T. The Nernst-Einstein conductivity is calculated by substituting these values together from the equation (2), and the ionicity is then obtained from the equation (3).

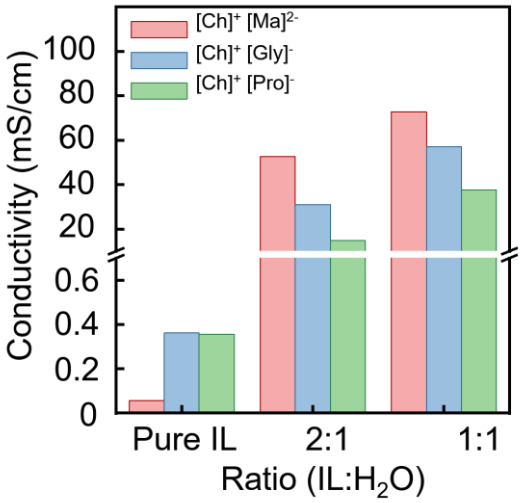
## Supplementary Figures



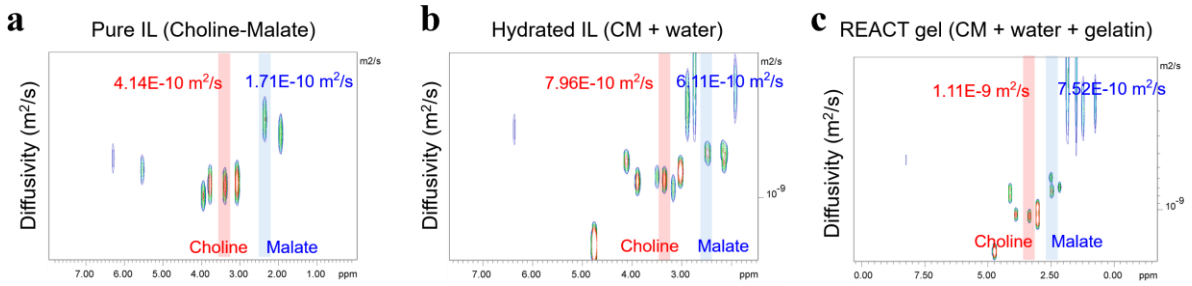

**Supplementary Figure 1. Schematic illustration comparing hydrogel, ion gel, and gelatin based REACT gel.** In the REACT gel, choline malate, water, and gelatin form a coupled hydrated ionic network. Unlike hydrogels and ion gels, the REACT gel uniquely combines high ion dissociation with suppression of ion and water leakage.



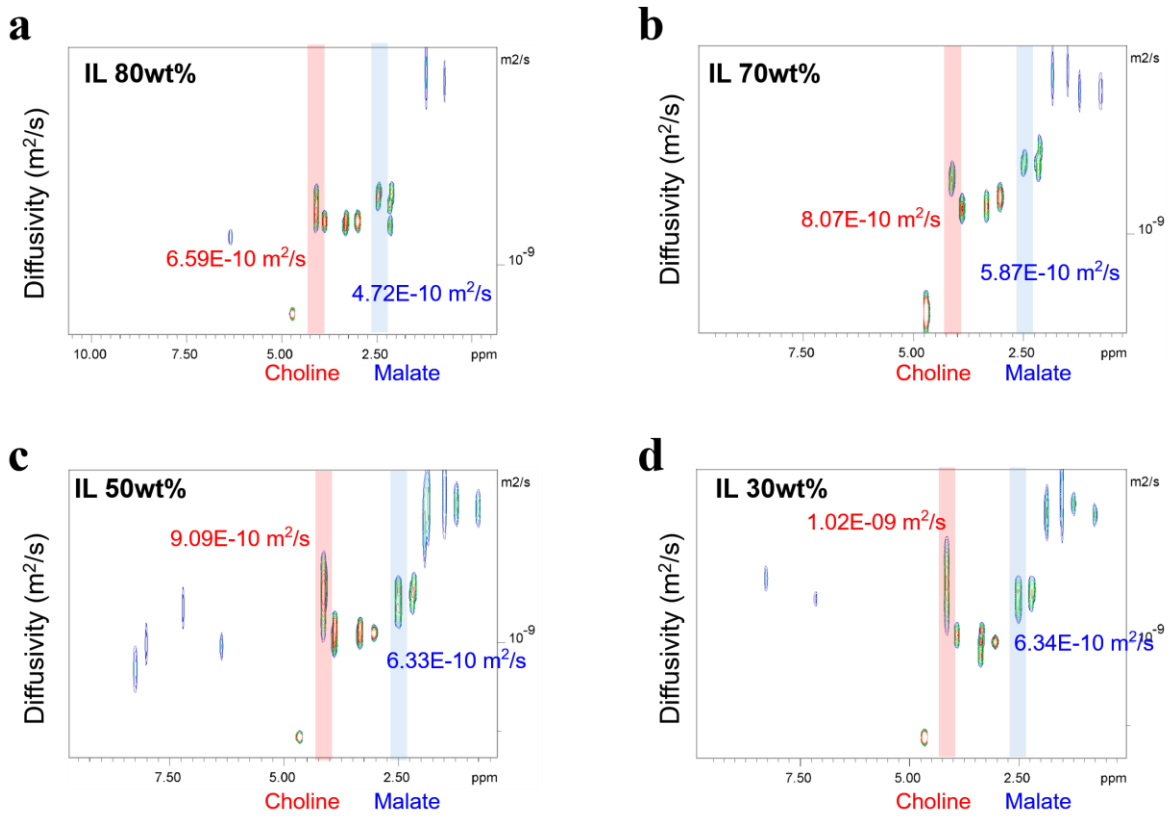

**Supplementary Figure 2. Molecular structures of the constituent materials for the REACT gel.**



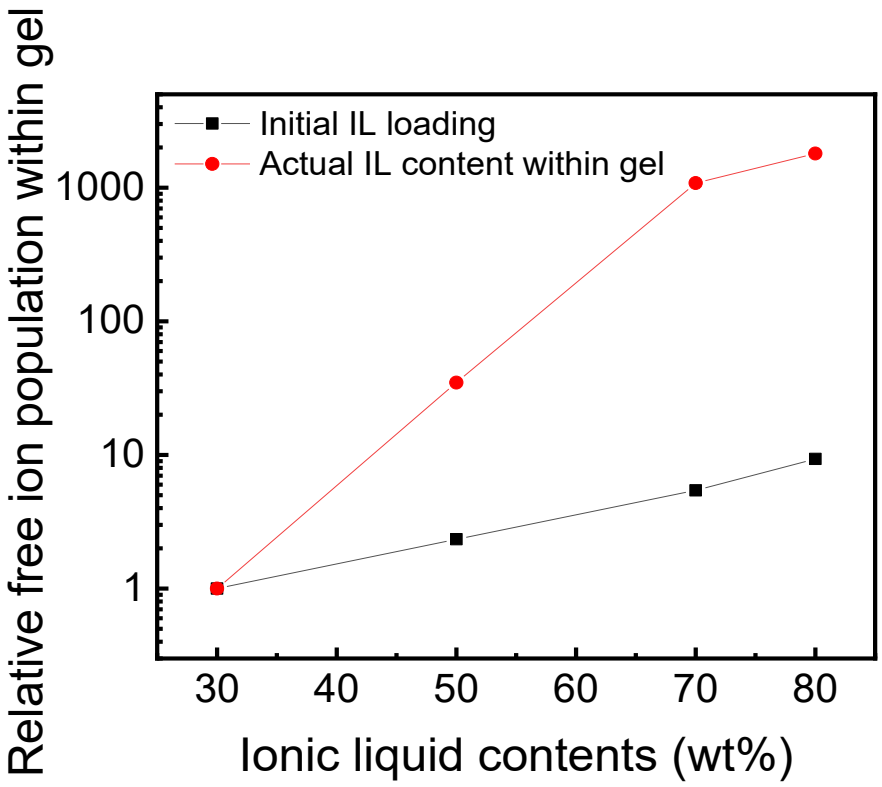

**Supplementary Figure 3. Water-content-dependent ionic conductivity of choline malate, choline glycolate and choline propionate ionic liquids**



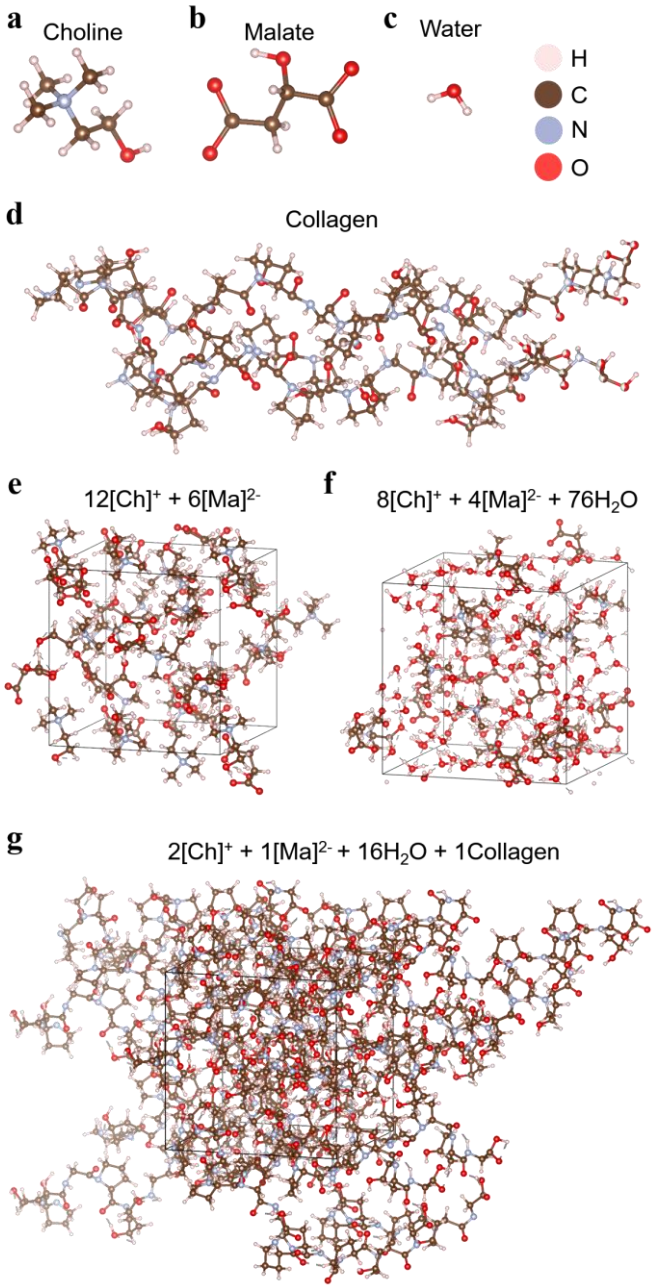

**Supplementary Figure 4. PFG-NMR analysis of ion diffusivity in pure choline malate (CM) ionic liquid (IL), hydrated CM and gelatin-based REACT gel.** PFG-NMR measurements of choline and malate ion diffusivity in (**a**) pure choline malate ionic liquid, (**b**) hydrated choline malate and (**c**) gelatin-based REACT gel. The malate and choline signals at approximately 2.4 and 3.4 ppm, respectively, were used to determine the diffusivity of each ionic species.



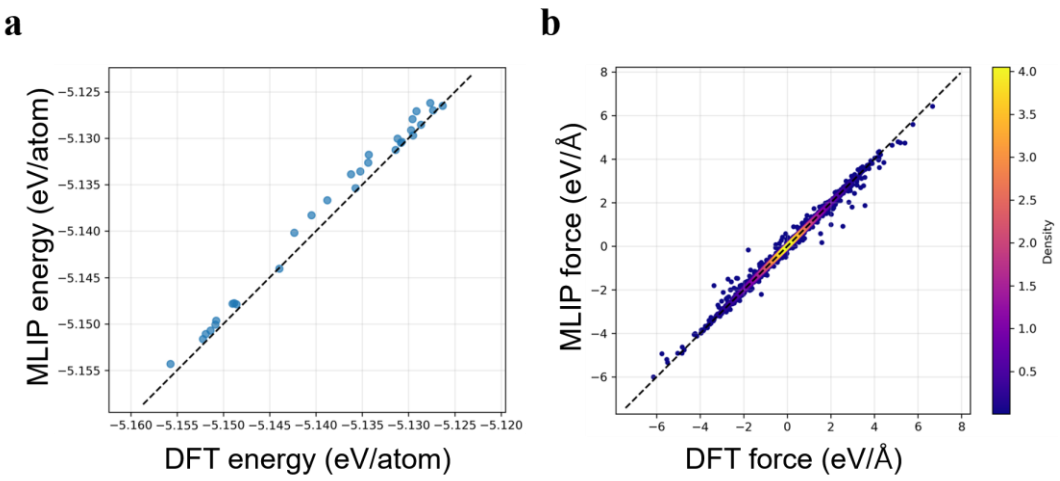

**Supplementary Figure 5. PFG-NMR-derived ion diffusivity in REACT gels with different ionic liquid contents.** PFG-NMR analysis of ion diffusivity in REACT gels containing (**a**) 80 wt%, (**b**) 70 wt%, (**c**) 50 wt% and (**d**) 30 wt% of choline malate ionic liquid.



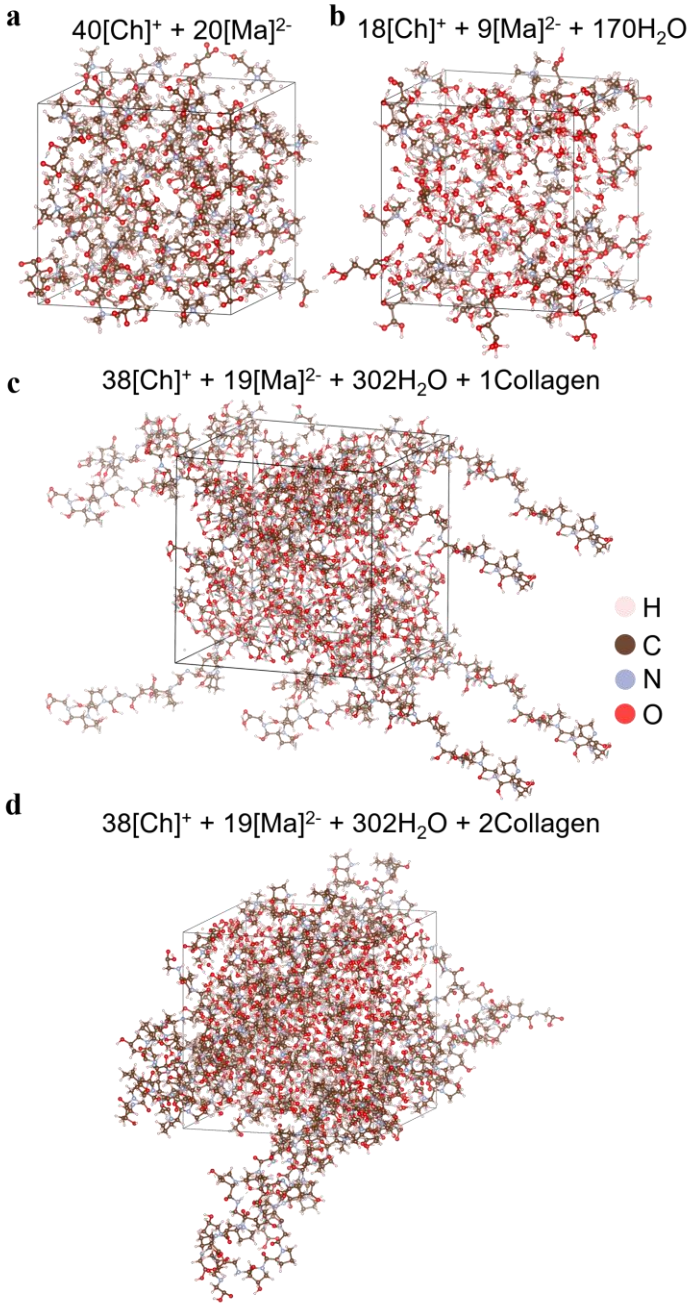

**Supplementary Figure 6. Gel-assisted amplification of free-ion population in REACT gels with increasing ionic liquid content**



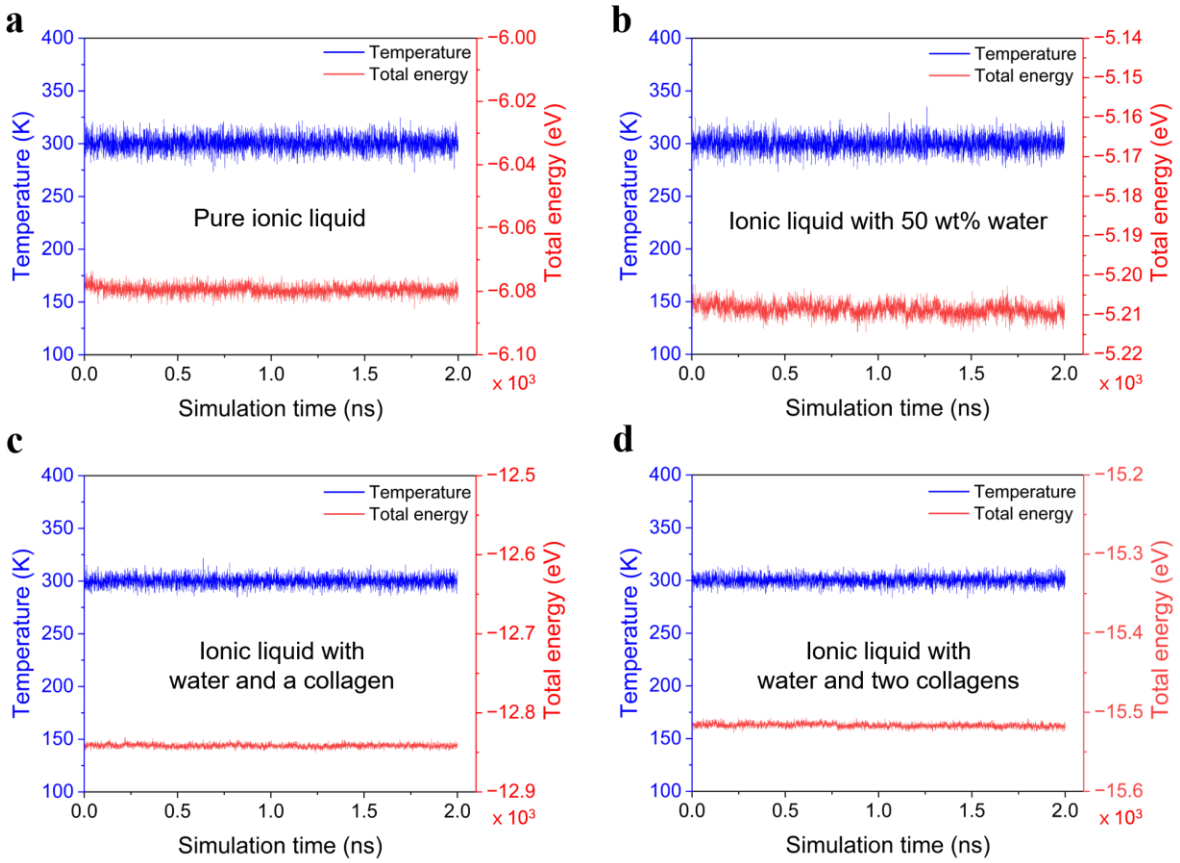

**Supplementary Figure 7. Representative molecular configurations and simulation cells used for on-the-fly MLFF training of choline malate ionic liquid, hydrated ionic liquid, and collagen-containing electrolyte systems.** The molecular configuration of (**a**) choline, (**b**) malate, (**c**) water, and (**d**) collagen models. Computational model for on-the-fly MLFF simulations of (**e**) $12[Ch]^{+} + 6[Ma]^{2-}$ (pure ionic liquid), (**f**) $8[Ch]^{+} + 4[Ma]^{2-} + 76H_2O$ (ionic liquid with 50 wt% $H_2O$), and (**g**) $2[Ch]^{+} + 1[Ma]^{2-} + 16H_2O$ + 1Collagen (ionic liquid with water and collagen). Pink, brown, light blue, and red spheres indicate H, C, N, and O atoms, respectively. $[Ch]^{+}$ and $[Ma]^{2-}$ represent choline cation and malate anion, respectively.



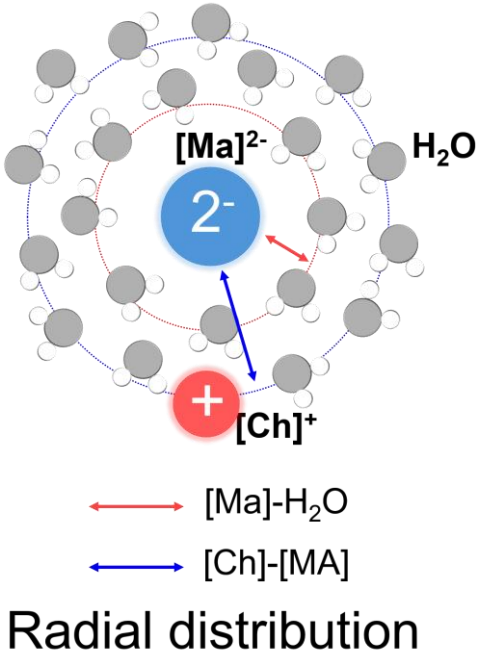

**Supplementary Figure 8. Parity plots demonstrate the alignment between DFT and MLIP predictions for energies and atomic forces in the hydrated choline malate ionic liquid model.** The parity plot between DFT and MLIP calculations of (**a**) energy (eV/atom) and (**b**) forces (eV/Å) on $8[Ch]^{+} + 4[Ma]^{2-} + 76H_2O$ (ionic liquid with 50 wt% $H_2O$) model (Fig. S7f)**.**



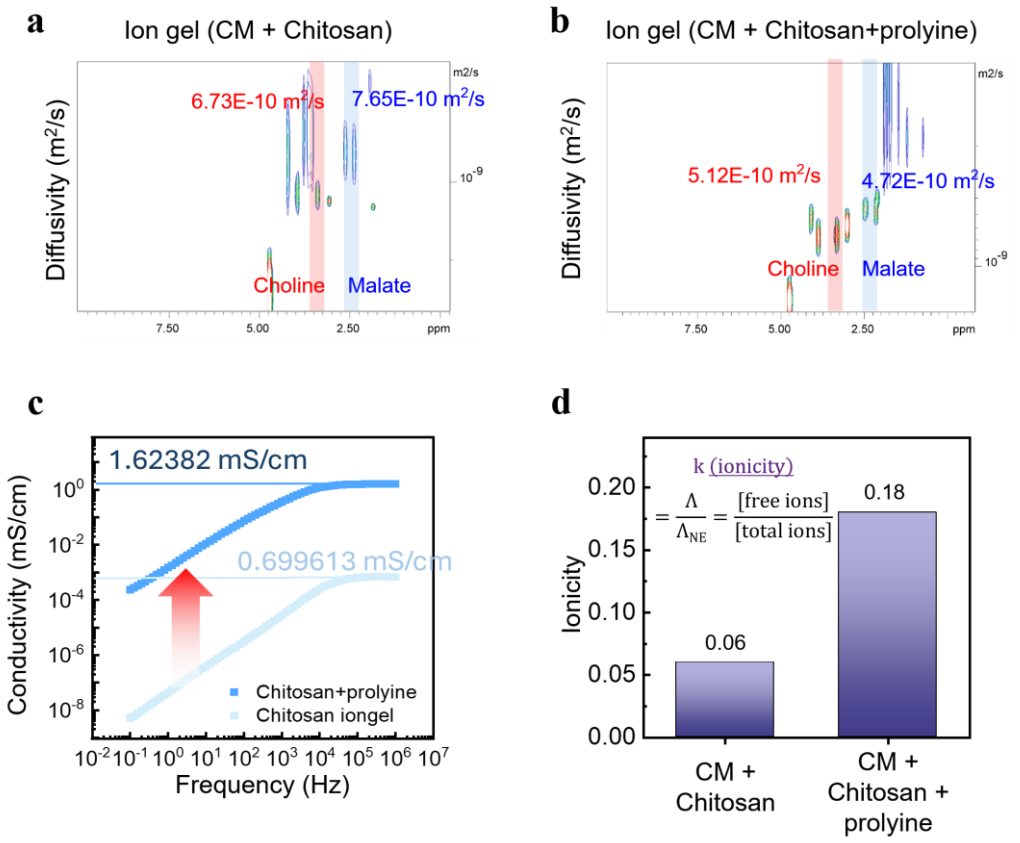

**Supplementary Figure 9. Representative MLIP simulation cells constructed to examine the effects of hydration and collagen incorporation on the ion dissociation and transport in choline malate ionic liquid systems**. The computational model for MLIP simulations of (**a**) 40$[Ch]^+$ + 20$[Ma]^{2-}$ (pure ionic liquid), (**b**) 18$[Ch]^+$ + 9$[Ma]^{2-}$ + 170$H_2O$ (ionic liquid with 50 wt% $H_2O$), (**c**) 38$[Ch]^+$ + 19$[Ma]^{2-}$ + 302$H_2O$ + 1Collagen (ionic liquid with water and collagen molecule), and (**d**) 38$[Ch]^+$ + 19$[Ma]^{2-}$ + 302$H_2O$ + 2Collagen (ionic liquid with water and two collagen molecules). Pink, brown, light blue, and red spheres indicate H, C, N, and O atoms, respectively. $[Ch]^+$ and $[Ma]^{2-}$ represent choline cation and malate anion, respectively.



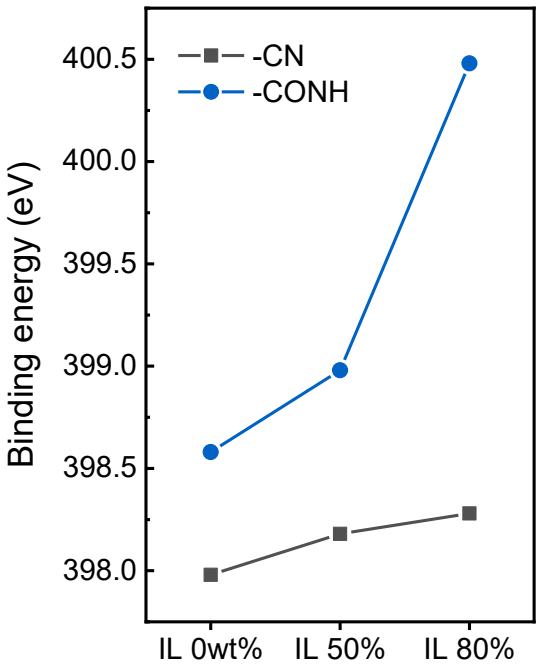

**Supplementary Figure 10. Temporal profiles of temperature and total energy confirming stable NVT dynamics for the pure, hydrated, and collagen-containing choline malate ionic liquid systems.** Total energy (eV) and temperature (K) data of (**a**) pure ionic liquid (IL), (**b**) ionic liquid with 50 wt% water (hydrated IL), (**c**) ionic liquid with water and a collagen (3 gelatin chains), and (**d**) ionic liquid with water and two collagen molecules models for 2 ns NVT simulation with 0.5 fs timestep. Blue and red line indicate total energy and temperature, respectively.



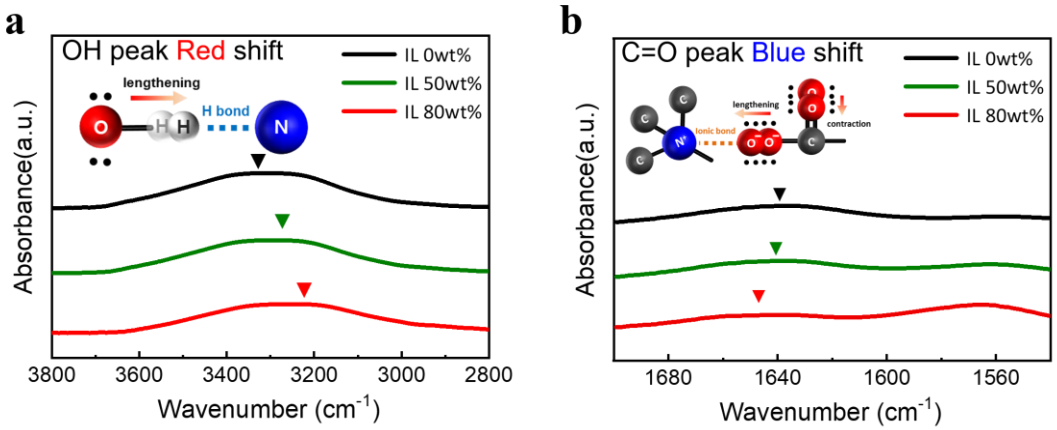

**Supplementary Figure 11. Schematic illustration of radial distribution functions (RDFs) for $[Ma]^{2-}$-$H_2O$ and [Ch]-[MA] pairs.**



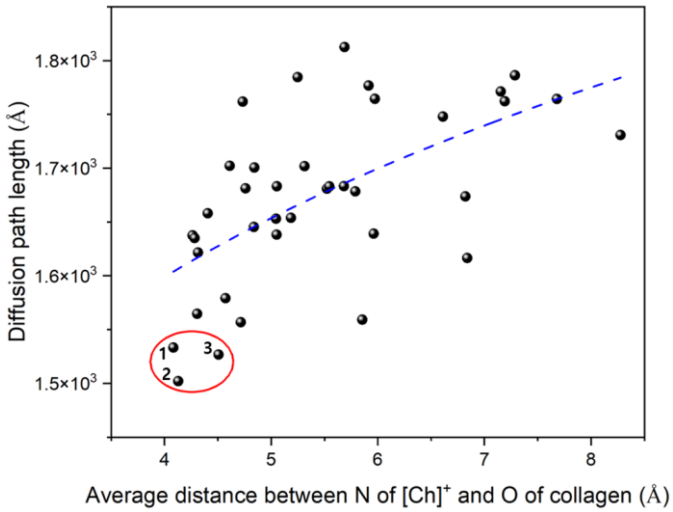

**Supplementary Figure 12. Generality of amino-acid-assisted ion decarboxylation in chitosan ion gels.** PFG-NMR analysis of choline malate ion diffusivity in (**a**) chitosan ion gel and (**b**) proline-incorporated chitosan ion gel. (**c**) Ionic conductivity of chitosan ion gels with and without proline. (**d**) Comparison of ionicity values calculated from ion diffusivity and ionic conductivity, showing that proline addition enhances ion dissociation in the chitosan matrix.



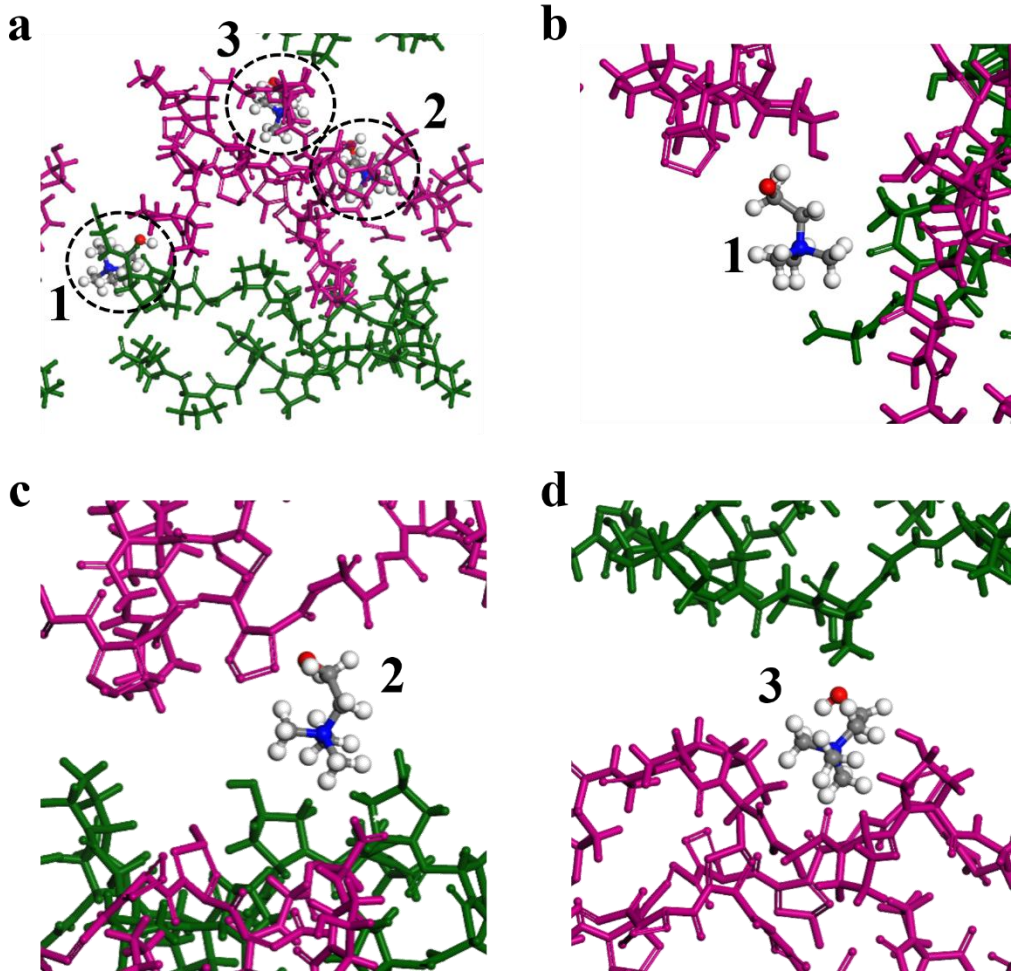

**Supplementary Figure 13. XPS analysis of REACT gels with different ionic liquid contents.** XPS spectra of REACT gels with increasing choline malate ionic liquid content. The peaks shift toward higher binding energy with increasing ionic liquid content, indicating strengthened interactions between the ionic liquid and the gelatin matrix.




**Supplementary Figure 14. FT-IR analysis of REACT gels with different ionic liquid contents.** (**a**) O-H stretching and (**b**) C=O stretching regions of REACT gels with different ionic liquid contents. The O-H peak shifts to lower wavenumbers with increasing ionic liquid content, reflecting enhanced hydrogen bonding among gelatin, CM and water. By contrast, the C=O peak shifts to higher wavenumbers, indicating a strengthened local bonding environment around carbonyl groups through interactions between CM and the gelatin matrix.

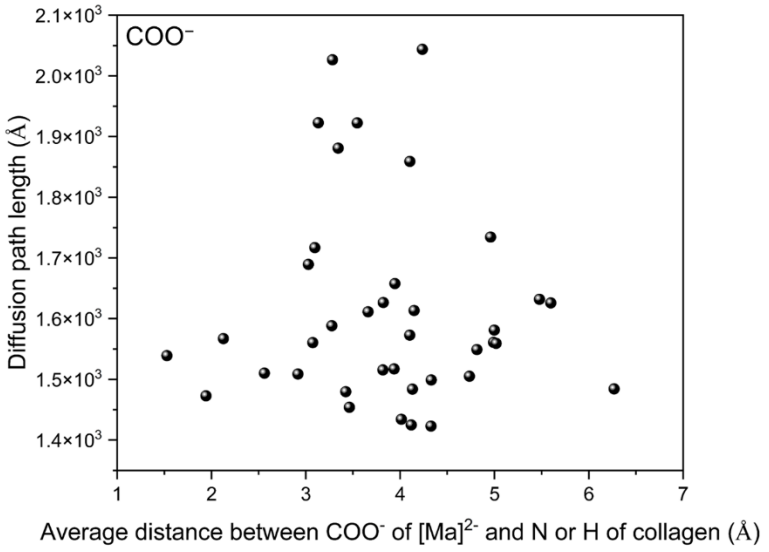



**Supplementary Figure 15. Distance-dependent mobility analysis shows that $[Ch]^+$ ions located closer to collagen oxygen atoms exhibit suppressed diffusion, indicating interfacial confinement by the collagen matrix.** Diffusion path length (Å) of N atom of $[Ch]^+$ and averages distance (Å) between N atom of $[Ch]^+$ and O of collagen molecules during 2 ns of NVT simulation. The points labeled 1, 2, and 3 correspond to the most immobilized ions localized in interstitial voids between adjacent collagen helices.

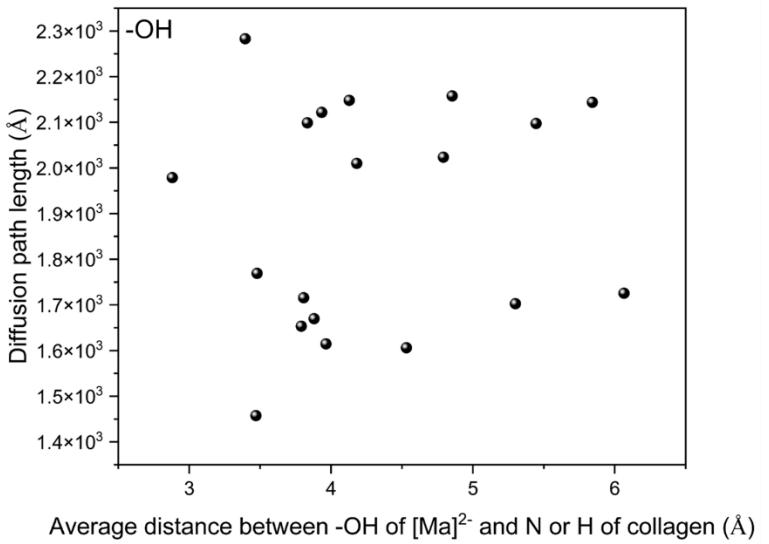



**Supplementary Figure 16. Local configurations of $[Ch]^+$ ions confined within interstitial collagen environments, highlighting their potential role as electrostatic bridges between neighboring collagen molecules.** Configurations of the $[Ch]^+$ ions and surrounding collagen molecules after a 2 ns NVT simulation. The labels 1, 2, and 3 correspond to the sites marked in Fig. S14. (**a**) Overview of the three $[Ch]^+$ positions within the collagen matrix. (**b–d**) Magnified views of the local environments for positions 1, 2, and 3, respectively. Pink, brown, light blue, and red spheres denote H, C, N, and O atoms, respectively. Purple and green sticks represent distinct collagen molecules.

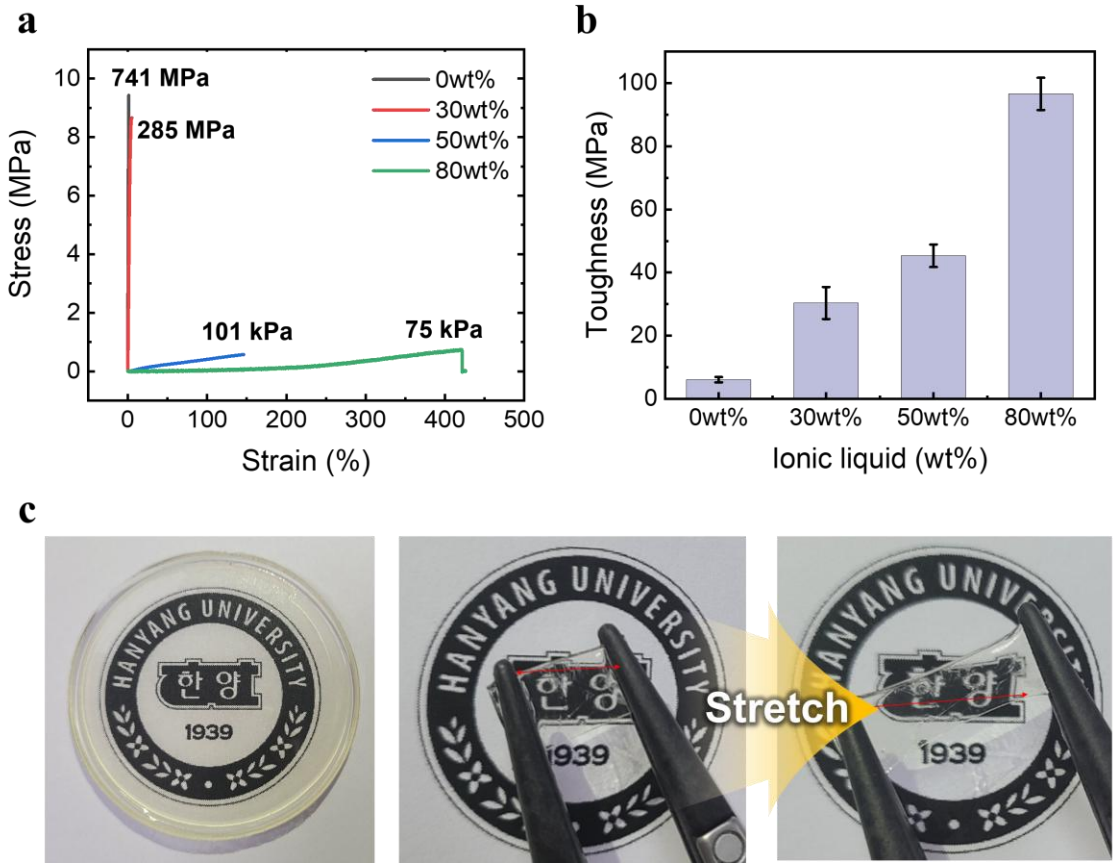
**a**



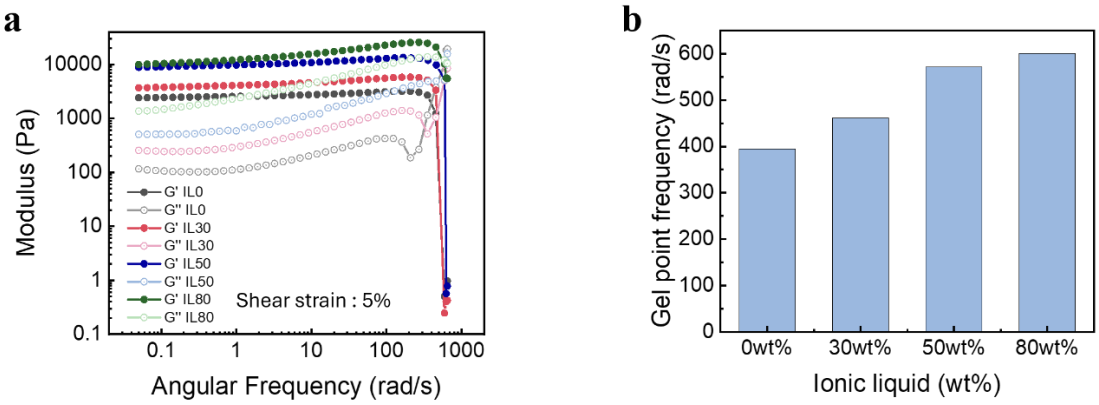

**b**



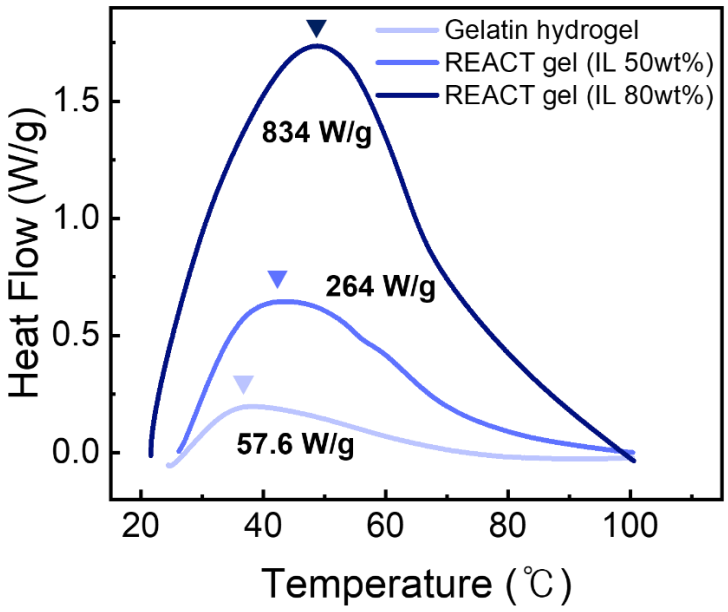

**Supplementary Figure 17**. **Mobility-distance correlation analysis showing that $[Ma]^{2-}$ functional groups exhibit no clear interstitial confinement with collagen, unlike the localized anchoring behavior observed for $[Ch]^{+}$ ions.** Diffusion path length (Å) as a function of the average distance (Å) between the N or H atoms of collagens and the (**a**) center of mass of the $COO^{-}$ groups, and (**b**) O atom of the -OH group in $[Ma]^{2-}$ during a 2 ns NVT simulation.




**Supplementary Figure 18. Mechanical properties of REACT gels with different ionic liquid contents.** (**a**) Stress-strain curves of REACT gels with different ionic liquid contents. As the ionic liquid content increases, the modulus decreases, while the gels become more stretchable. (**b**) Toughness comparison of REACT gels with different ionic liquid contents. Although the gels become softer at higher ionic liquid contents, their toughness increases due to enhanced internal interactions and energy dissipation, making them more suitable for stretchable electronic devices. (**c**) Photograph of the REACT gel with 80 wt% ionic liquid, showing high transparency and stretchability.

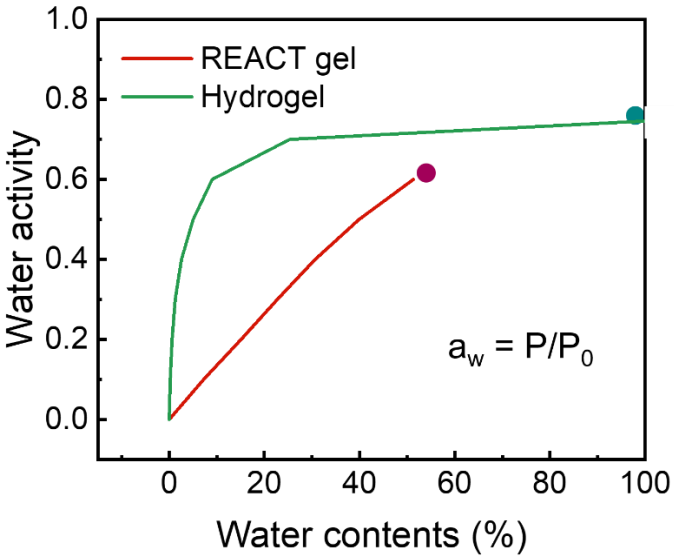



**Supplementary Figure 19. Rheological analysis of internal interactions and viscoelastic properties of REACT gels.** (**a**) Frequency-dependent dynamic storage modulus, G′, shown as filled circles, and loss modulus, G″, shown as open circles, of REACT gels with different ionic liquid contents. (**b**) Comparison of the crossover frequencies of the modulus curves, which are regarded as the gel-point of REACT gels with different ionic liquid contents. A higher gel-point frequency indicates stronger internal network interactions and improved mechanical stability of the gel structure.

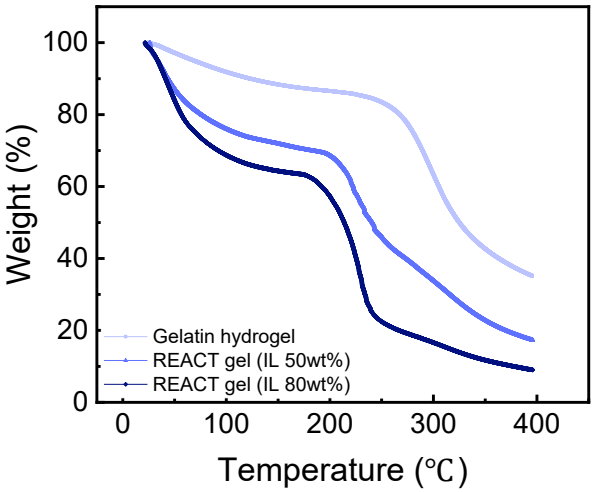



**Supplementary Figure 20. DSC analysis of REACT gels with different ionic liquid contents.** Denaturation temperature and enthalpy of REACT gels with different ionic liquid contents, showing enhanced thermal stabilization of the gelatin matrix with increasing ionic liquid content.

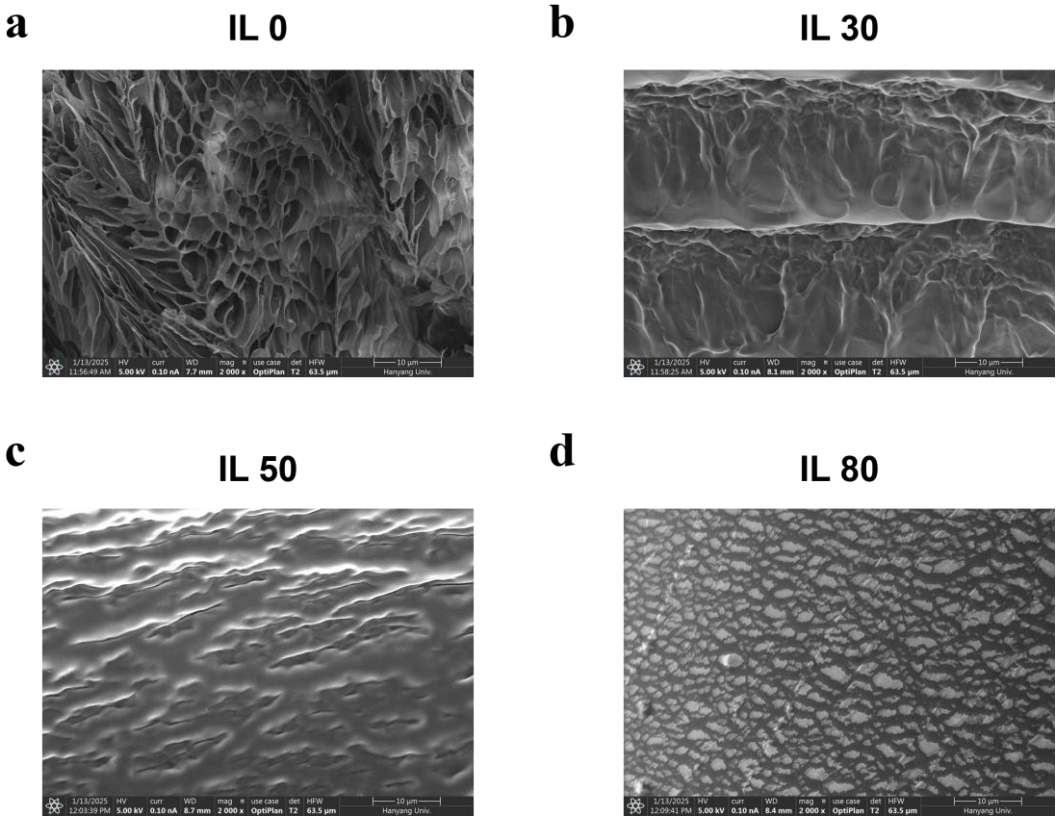
.




**Supplementary Figure 21. Water activity of PEO-based hydrogel and REACT gel.** Water activity is derived from DVS isotherms across the relative humidity range. The REACT gel exhibits consistently lower water activity than the PEO-based hydrogel, indicating reduced chemical potential of water and suppressed moisture exchange with the surrounding environment.

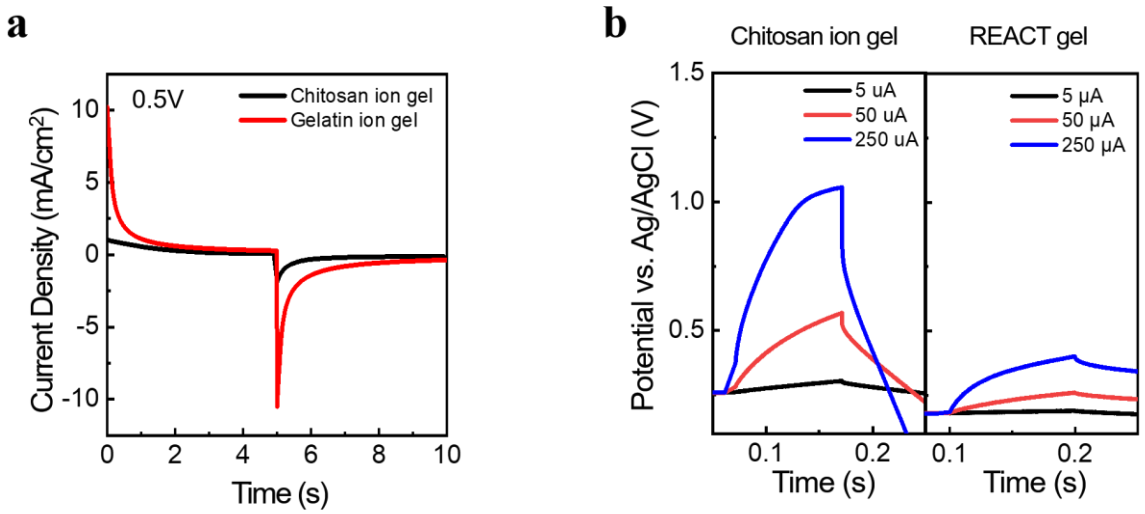



**Supplementary Figure 22. TGA analysis of water retention in REACT gels with different ionic liquid contents.** Thermogravimetric analysis (TGA) profiles of REACT gels with different ionic liquid contents after two weeks of storage. The REACT gel with higher ionic liquid content retains a larger residual weight, indicating enhanced water retention and improved dehydration resistance through stronger water anchoring within the gelatin-CM network.

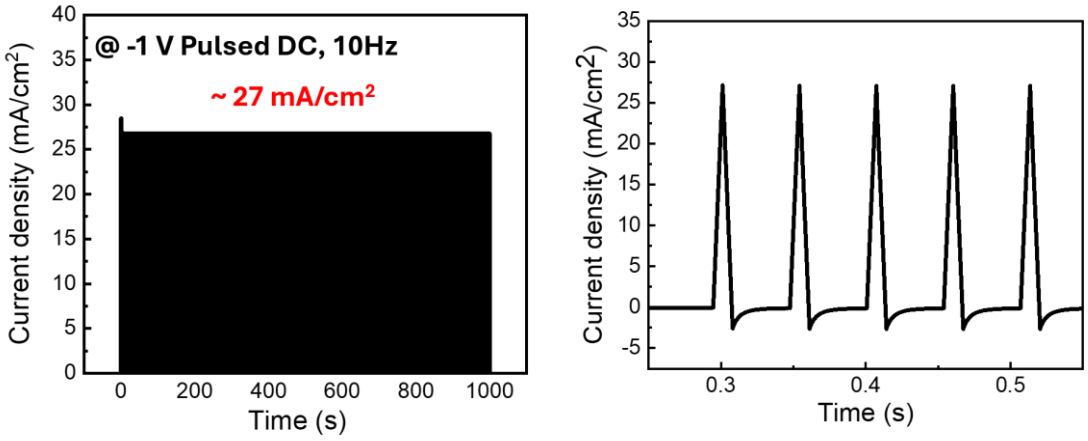



**Supplementary Figure 23. SEM images of REACT gels with different ionic liquid contents.**

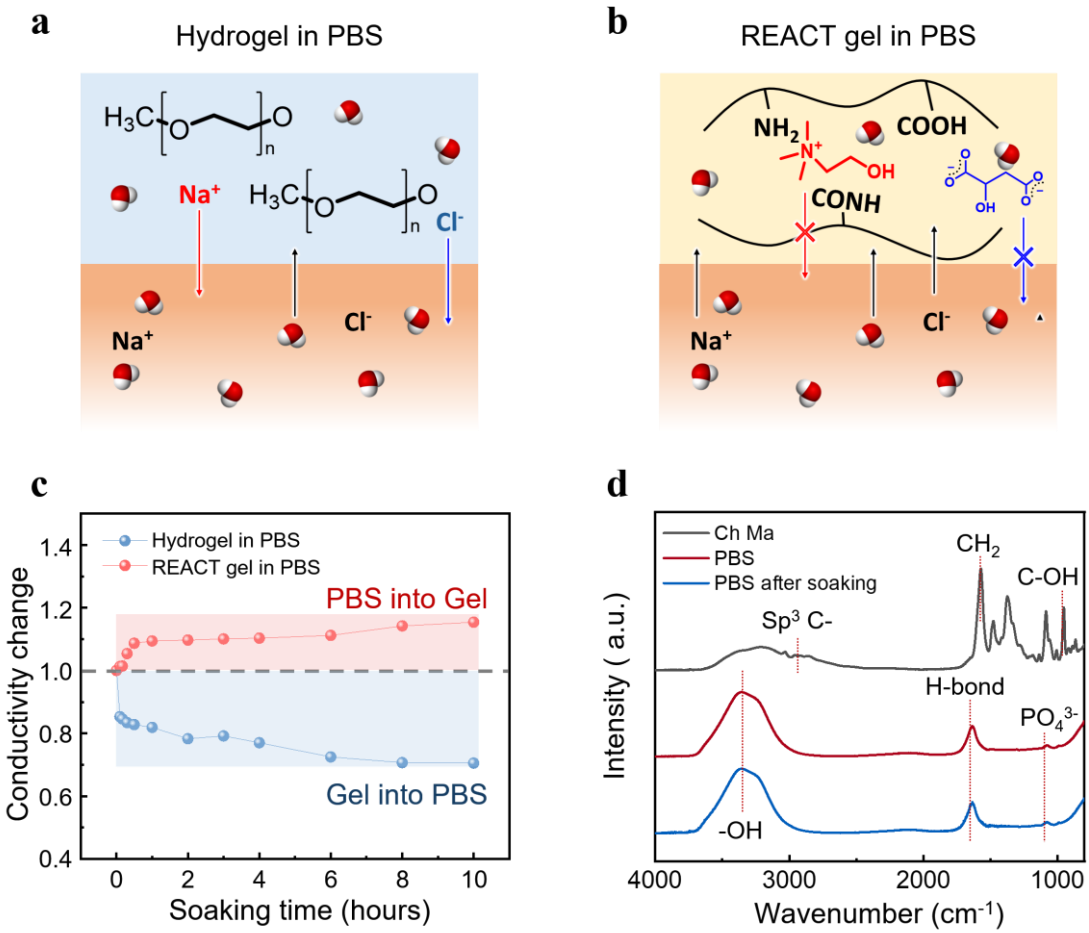
SEM images of REACT gels containing choline malate ionic liquid at (**a**) 0 wt%, (**b**) 30 wt%, (**c**) 50 wt% and (**d**) 80 wt%. Gels with lower ionic liquid contents show highly porous structures due to substantial water evaporation, whereas gels with higher ionic liquid contents exhibit denser and nearly pore-free morphologies, indicating enhanced water retention within the gelatin-CM network.



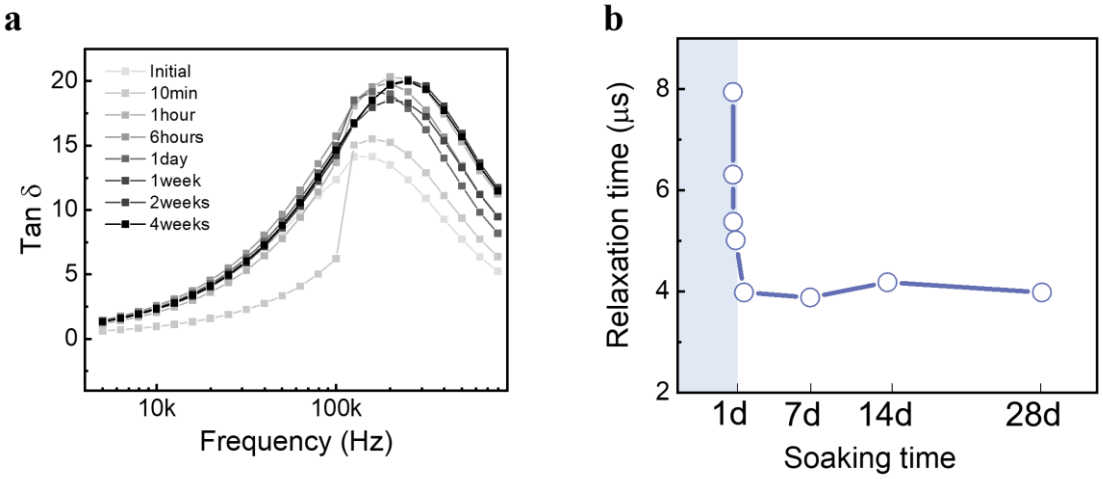

**Supplementary Figure 24. Electrochemical performance of chitosan ion gel and REACT gel.** (**a**) Chronoamperometric current-density response of the chitosan ion gel and REACT gel under an applied bias of 0.5 V. (**b**) Chronopotentiometric voltage response required to sustain the same current. The REACT gel shows a higher current density and requires a lower operating voltage than the chitosan ion gel, demonstrating its efficient low-voltage ionic conduction.



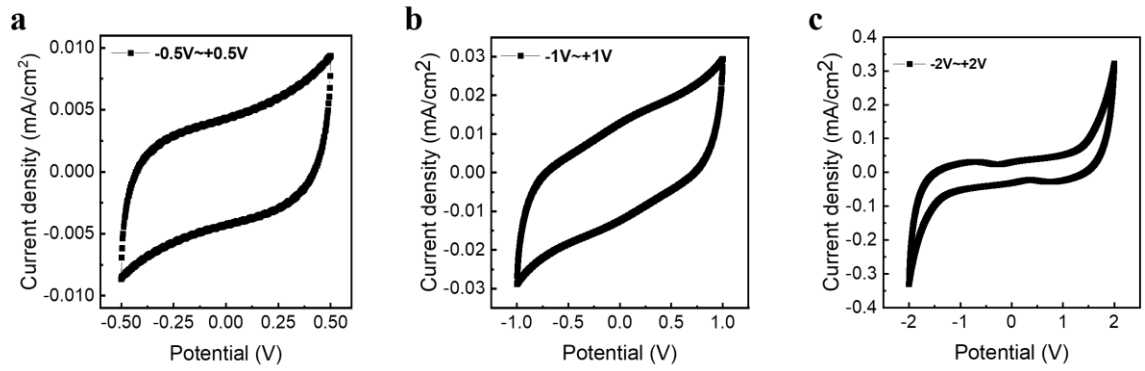

**Supplementary Figure 25. Current-density output of the REACT gel under DC pulsing.** Current-density response of the REACT gel under a 10 Hz DC pulse. The REACT gel stably generates a high current density of approximately 27 mA $cm^{-2}$, demonstrating its capability as an efficient ionic conductor for pulsed electrical operation.



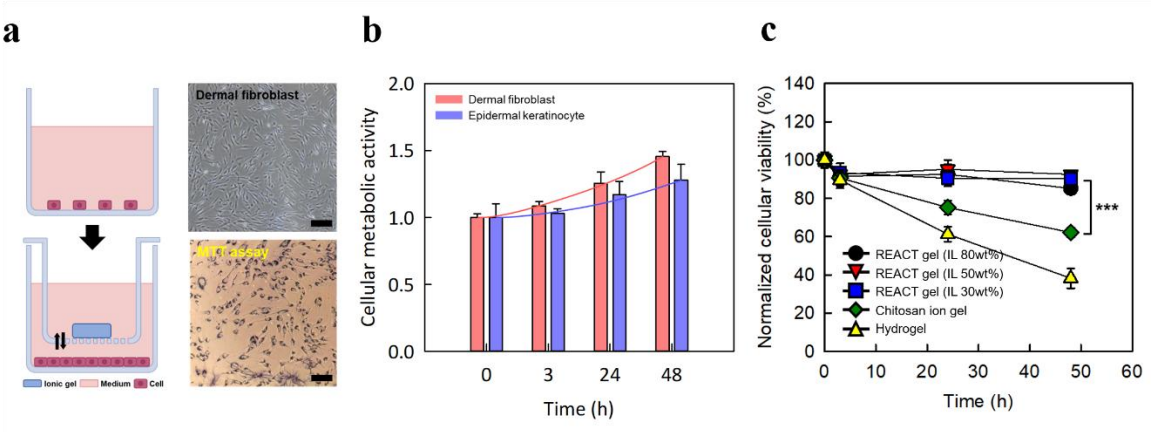

**Supplementary Figure 26. Ion-leakage behavior of conventional hydrogel and REACT gel in PBS.** (**a-b**) Schematic illustrations of ion migration in a conventional ion-conducting hydrogel and the REACT gel during PBS soaking. In the conventional hydrogel, ions diffuse from the gel into PBS, whereas the REACT gel suppresses CM leakage and allows PBS ions to permeate into the gel. (**c**) Ionic conductivity changes of the conventional hydrogel and REACT gel after PBS soaking. (**d**) FT-IR spectra of PBS after immersion, showing no detectable CM peaks from the REACT gel after 1 day of soaking.



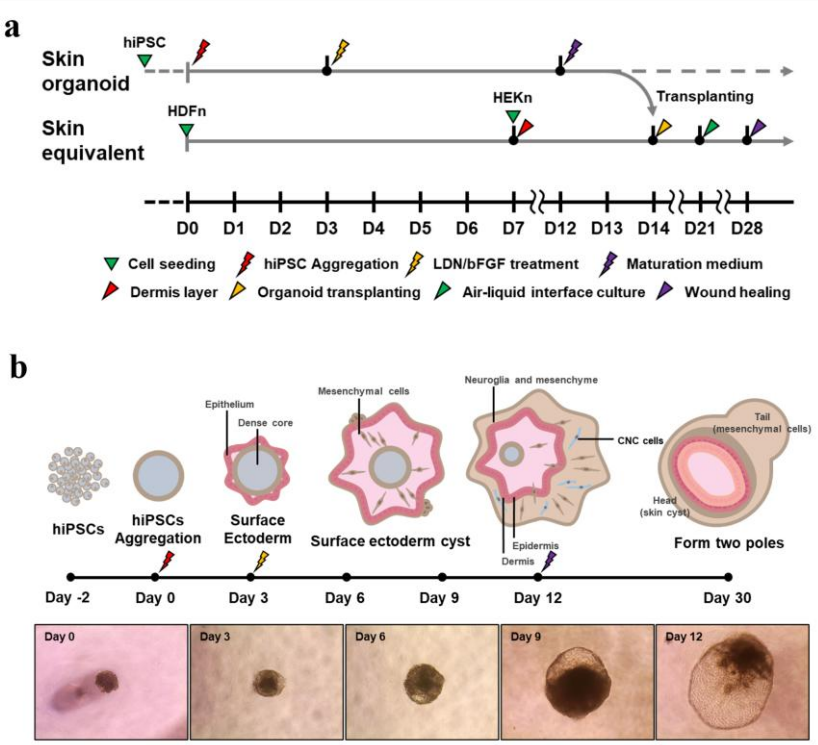

**Supplementary Figure 27. Long-term electrical sustainability of the REACT gel during PBS soaking.** (**a**) Frequency-dependent tan δ spectra of the REACT gel during PBS soaking for one month. (**b**) Extracted free-ion-related parameter as a function of soaking time, showing stable ionic behavior after the initial soaking period.



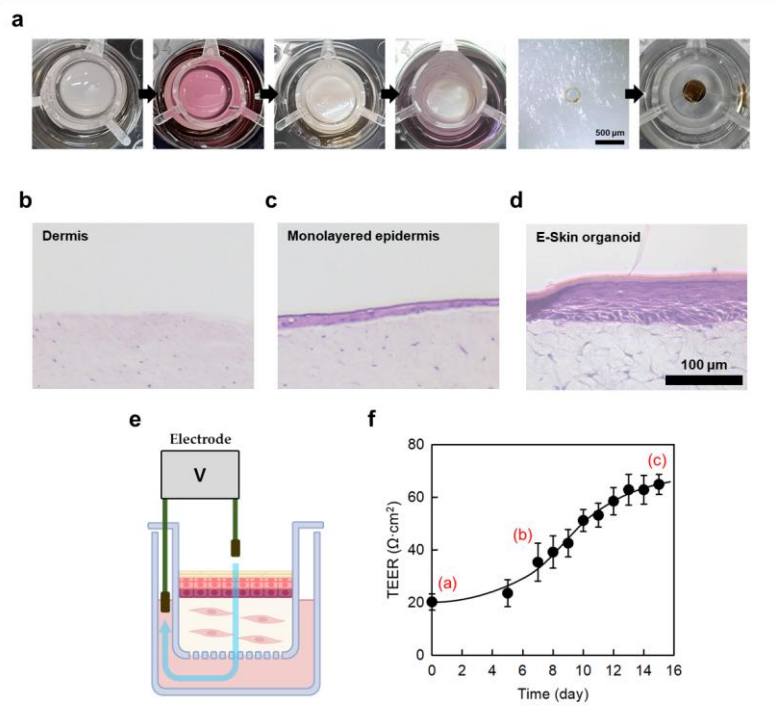

**Supplementary Figure 28. Electrochemical stability of the REACT gel.** Cyclic voltammetry curves of the REACT gel measured within voltage windows of (**a**) ±0.5 V, (**b**) ±1 V and (**c**) ±2 V, showing no obvious redox peaks and confirming stable electrochemical behavior over the applied voltage ranges.



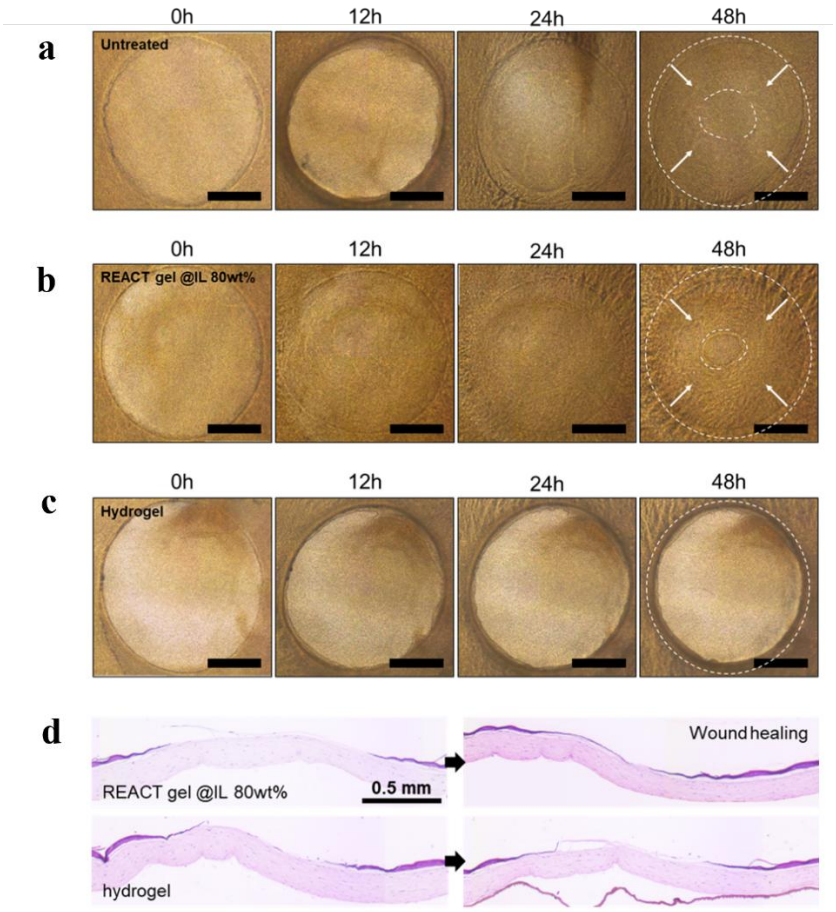

**Supplementary Figure 29. Cytocompatibility assessment of ionic gels.** (**a**) Schematic illustration of the Transwell-based exposure system used to evaluate the cytocompatibility of ionic gels. Ionic gel samples were placed in the insert chamber, allowing soluble components to interact with the underlying cells cultured on the bottom well. (**b**) Cellular metabolic activity of human dermal fibroblasts (HDFn) and human epidermal keratinocytes (HEKn) over 48 h, assessed by MTT assay. Representative microscopic images show formazan formation following MTT reduction. (**c**) Normalized cellular viability following exposure to different gel formulations, including REACT gels (IL30, IL50 and IL80), chitosan ion gel (IL50), and NaCl-containing hydrogel (3 M). While the hydrogel group exhibited a marked decrease in viability over time, gelatin-based ionic gels maintained high cellular viability throughout the 48 h exposure. Data are presented as mean ± s.d. ***P < 0.001.



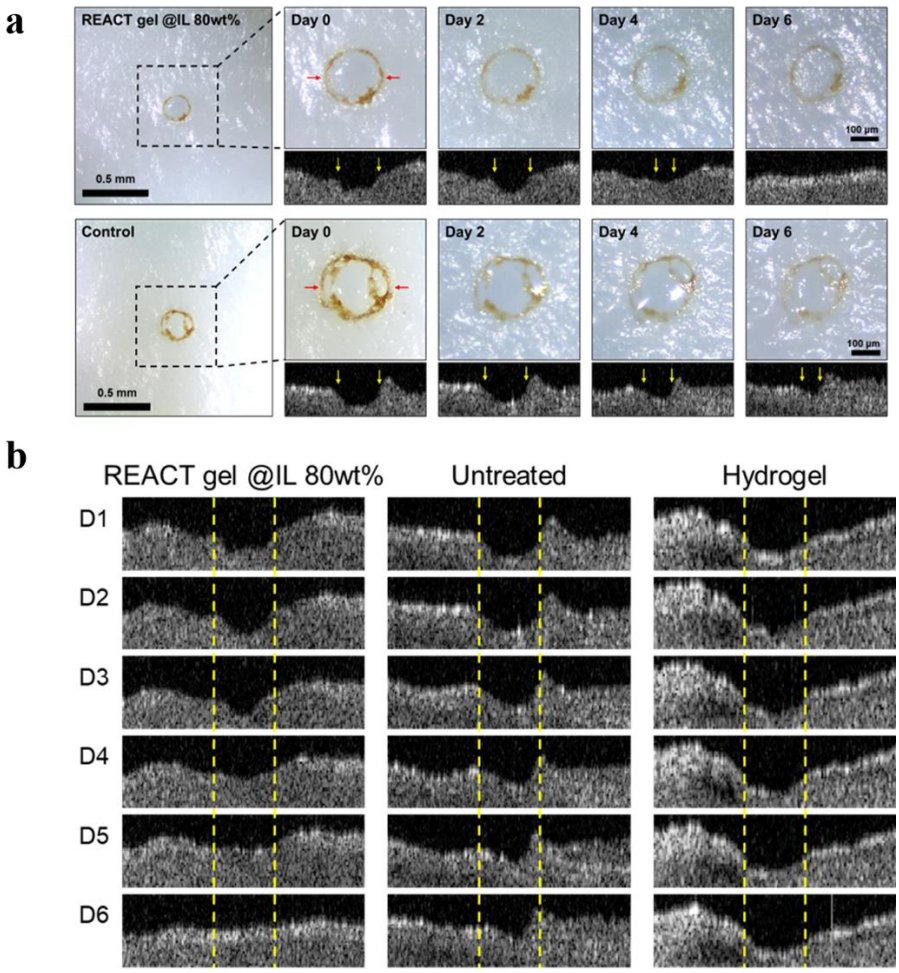

**Supplementary Figure 30. Differentiation and assembly of engineered skin organoids.** (**a**) Experimental timeline for the generation of engineered skin organoids (E-skin organoids). Human induced pluripotent stem cell (hiPSC)-derived skin organoids were differentiated for approximately 15 days before transplantation onto a dermal equivalent to construct the E-skin organoid platform. In parallel, a dermal matrix containing human dermal fibroblasts (HDFn) was prepared to form the skin equivalent scaffold. Human epidermal keratinocytes (HEKn) were subsequently seeded onto the dermal layer, followed by transplantation of the differentiated skin organoids. Epidermal stratification and maturation were induced through air-liquid interface culture, after which wound-healing experiments were conducted. (**b**) Stepwise differentiation process of skin organoids derived from hiPSCs. hiPSCs first formed spheroid aggregates that subsequently differentiated into surface ectoderm through the controlled modulation of developmental signaling pathways. Sequential treatment with morphogens, including BMP4, bFGF and the BMP inhibitor LDN-193189, guided the formation of surface ectoderm cysts containing epithelial and mesenchymal cell populations. As differentiation progressed, the organoids developed increasingly complex skin-like structures, including epidermal and dermal compartments as well as neural crest-derived mesenchymal components. Representative bright-field images show the morphological progression of organoid development from day 0 to day 12.



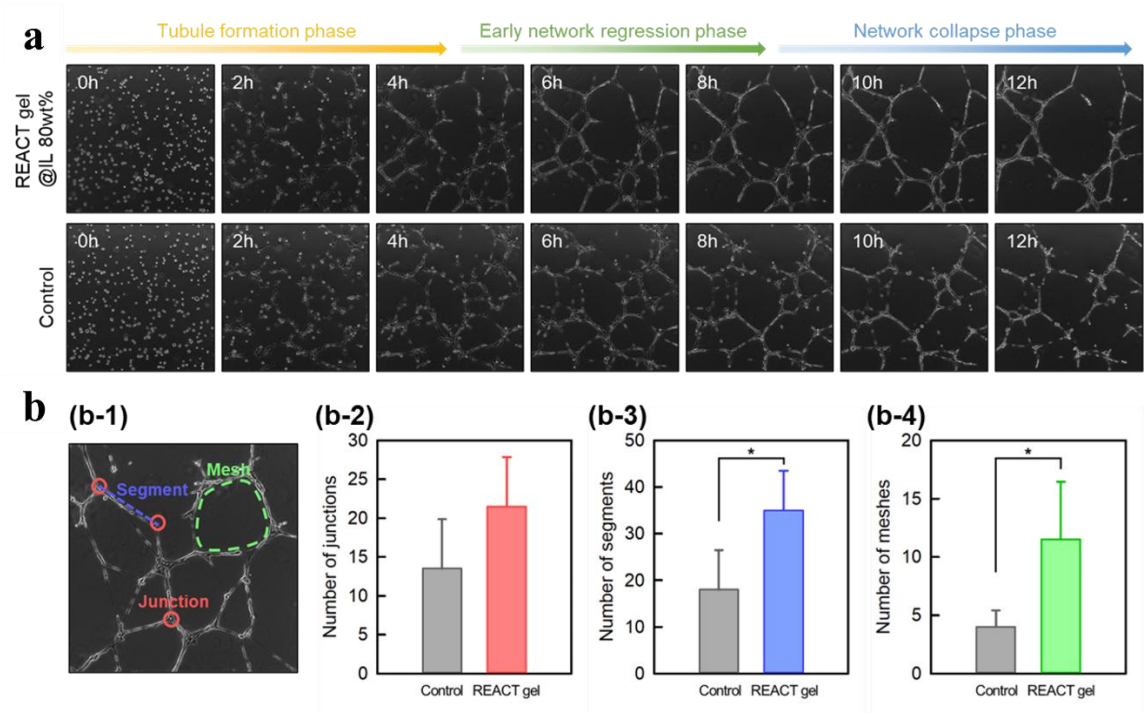

**Supplementary Figure 31. Structural maturation and barrier formation of engineered skin organoids monitored by TEER measurements.** (**a**) Representative photographs illustrating the fabrication process of the engineered skin organoid. (**b-d**) Histological characterization of the stepwise assembly of the engineered skin organoid (E-skin organoid). (**b**) Dermal equivalent composed of collagen matrix containing human dermal fibroblasts (HDFn). (**c**) Formation of a monolayered epidermis after seeding human epidermal keratinocytes (HEKn) onto the dermal layer. (**d**) Fully assembled E-skin organoid after air-liquid interface culture, showing a stratified epidermal structure resembling native skin tissue. Hematoxylin and eosin (H&E) staining confirms the progressive differentiation and organization of epidermal layers during the construction of the skin tissue model. (**e**) Schematic illustration of the transepithelial electrical resistance (TEER) measurement system used to non-invasively monitor epithelial barrier formation during the development of the E-skin organoid. Electrodes were placed in the apical and basal chambers of the culture insert to measure electrical resistance across the epidermal layer. (**f**) Time-dependent evolution of TEER values during E-skin organoid maturation. TEER gradually increased as the epidermal layer differentiated and formed a functional barrier. Resistance values reached a stable plateau after approximately 14 days of culture, indicating the establishment of a mature epidermal barrier. Fully matured E-skin organoids on day 14 were subsequently used for wound-healing experiments.




**Supplementary Figure 32. Wound healing dynamics in biopsy punch-injured E-skin organoids under different gel treatments.** (**a-c**) Time-lapse stereomicroscope images showing wound closure in E-skin organoids following biopsy punch-induced injury. Circular wounds were generated in the epidermal layer, and different gel formulations were applied to the wound region. (**a**) Untreated control. (**b**) REACT gel. (**c**) NaCl-containing hydrogel (2 M NaCl). Images acquired at 0, 12, 24 and 48 h show progressive re-epithelialization of the wound region. The ionic gel-treated group exhibited faster inward migration of epidermal cells and more efficient wound closure compared with the untreated control, whereas the hydrogel group showed delayed epithelial regeneration and impaired wound healing. Dashed circles indicate the original wound boundary, and arrows denote the direction of epidermal cell migration. (**d**) Histological evaluation of wound repair in E-skin organoids. Representative hematoxylin and eosin (H&E)-stained cross-sections reveal enhanced epidermal regeneration and tissue reconstruction in the ionic gel group, whereas incomplete closure and disrupted tissue morphology are observed in the hydrogel-treated samples.




**Supplementary Figure 33. OCT-based visualization of epidermal regeneration in laser-induced wounds of E-skin organoids.** (**a**) Representative optical and OCT images showing epidermal regeneration following laser-induced micro-wounding in E-skin organoids. Wounds were generated using a laser and the healing process was monitored over time in organoids treated with gelatin ionic gel containing 80% ionic liquid (REACT gel) or in untreated controls. Sequential images from day 0 to day 6 show progressive closure and re-epithelialization of the wound region. The gelatin ionic gel-treated group exhibited faster restoration of the epidermal layer compared with the control. (**b**) Time-resolved OCT cross-sectional images of the wound region in E-skin organoids treated with REACT gel, untreated controls, or NaCl-containing hydrogel. The dashed lines indicate the boundaries of the wound area. The ionic gel-treated group showed more rapid reconstruction of the epidermal architecture, whereas delayed regeneration was observed in the untreated and hydrogel groups. These qualitative observations correspond to the quantitative analysis of epidermal regeneration presented in Fig. 5C.




**Supplementary Figure 34. Enhanced angiogenic activity induced by ionic gel during HUVEC tubular formation.** (**a**) Time-lapse live-cell imaging of HUVEC tubular formation on Matrigel following treatment with conditioned media derived from the wound-healing model. Representative images show the dynamic process of vascular network formation over 12 h in the control and REACT gel groups. The tubular formation process can be divided into three stages: initial tubule formation, early network regression, and network collapse. The ionic gel group maintained more stable and interconnected vascular networks compared with the control. (**b**) Quantitative analysis of vascular network structures using the angiogenesis analyzer in ImageJ. (**b-1**) Representative image illustrating the definitions of junction, segment, and mesh structures used for quantification. The numbers of junctions (**b-2**), segments (**b-3**), and meshes (**b-4**) were quantified at 12 h. Compared with the control group, conditioned media from the ionic gel-treated wound model significantly enhanced vascular network formation and stability in HUVEC cultures. Data are presented as mean ± s.d. *P < 0.05.

# Supplementary Tables

| References | Material | Ion conductivity at RT | Conductivity retention at RT | Application |
|---|---|---|---|---|
| | **Hydrogel** | | | |
| [22] | PVA / $H_2SO_4$ | 210 mS/cm | 3 days | Healing patch |
| [23] | PIVA / $Zr^{4+}$ | 11.47 mS/cm | 30 days | Tactile sensor |
| [24] | SCG-Zn | 35.75 mS/cm | 14 days | Supercapacitor |
| [25] | SBMA / MAA / SA | 4.9 ± 0.5 mS/cm | 45 days | Temperature sensor |
| [26] | PAD-SC | 43.2 mS/cm | 5 days | Supercapacitor |
| [27] | PVA / Cellulose / LiCl | 61.2 mS/cm | 30 days | Temperature sensor |
| [28] | P(MEDSAH-co-AA) / LiCl | 23.5 mS/cm | 16 months | Piezoelectret sensor |
| | **Ion gel** | | | |
| [29] | P([MATAC][TFSI]-co-HFBA) | 0.044 mS/cm | 29 days | Ionic skin |
| [30] | P(BA-co-PEGMA) | 32.3 mS/cm | 7 days | Pressure sensor |
| [31] | PVDF / COF / [BMIM][$TF_2N$] | 1.68 mS/cm | 30 days | Pressure sensor |
| [32] | P(EA-co-AA) | 0.55 mS/cm | 30 days | Temperature sensor |
| [33] | TPU / [TFSI][Li] | 0.49 mS/cm | 30 days | Pressure sensor |
| [34] | EG / SBMA | 1.31 mS/cm | 14 days | Soft robot |
| [35] | PVDF / [EMIM][DCM] / Ethanol / NaTFSI / SiO2 | 43.7 mS/cm | 15 days | Capacitor |
| [36] | PAA / TO-CNFs / [BMIM]Cl / AlCl3 | 0.7 ± 0.06 mS/cm | 30 days | Wearable sensor |
| [37] | PVA / [EMIM][ES] | 0.2 mS/cm | 10 days | Robotik skin |
| [38] | [VBIm][BF4] / Ph-3MVIm-BF4 / [C6-VIm2][(BF4)2] / [BMIM][$NTf_2$] | 0.97 mS/cm | 30 days | Artificial skin |
| | **Eutectogel** | | | |
| [39] | P(AA-co-HEA) / IPEI / ChCl / EG | 2.7 ± 0.1 mS/cm | 30 days | Motion sensor |
| [40] | PAA / PVP / ChCl / EG | 0.792 mS/cm | 30 days | Pressure sensor |
| [41] | PVA / ChCl / Gly | 18 mS/cm | 12 days | Strain sensor |
| [42] | PVA / LiCl / $ZnCl_3$ / EG | 19.7 mS/cm | 30 days | Strain sensor |

**Table S1.** Comparison of representative ion-conducting gels reported in previous studies. The materials are classified into hydrogels, ion gels, and eutectogels, and their ionic conductivity at room temperature, conductivity retention at room temperature, and corresponding applications are summarized. RT denotes room temperature.

| System | D ($cm^2/s$) / $10^{-7}$ | | |
|---|---|---|---|
| | $[Ch]^+$ | $[Ma]^{2-}$ | $H_2O$ |
| Pure IL | 0.622 | 0.358 | - |
| IL + $H_2O$ | 8.206 | 4.170 | 19.10 |
| IL + $H_2O$ + 1 collagen | 20.918 | 7.732 | 17.61 |

**Table S2.** Calculated diffusion coefficients for the pure IL, IL with $H_2O$ (IL + $H_2O$), and IL + $H_2O$ with a collagen molecule (IL + $H_2O$ + 1 collagen) system. The specific compositions correspond to those analyzed in Fig. S7**.**

| State | Number of Molecules | Pure IL | IL + $H_2O$ | IL + $H_2O$ + 1 collagen |
|---|---|---|---|---|
| Initial | $[Ch]^+$ | 40 | 18 | 38 |
| | $[Ma]^{2-}$ | 20 | 9 | 19 |
| Final | $[Ch]^+$ | 40 | 18 | 38 |
| | $[Ma]^{2-}$ | 17 | 6 | 1 |
| | $C_4$ | 1 | 1 | 1 |
| | $C_3$ | 0 | 2 | 9 |
| | $C_2$ | 3 | 0 | 12 |
| | $C_1$ | 2 | 2 | 17 |

**Table S3.** Changes in molecular counts before (Initial) and after (Final) the 2 ns NVT simulation for the pure IL, IL + $H_2O$, and IL + $H_2O$ + 1 collagen system. The specific initial compositions correspond to those analyzed in Fig. S7. $C_n$ (n=1~4) denotes a molecule consisting of n carbon atoms.

## References


1. Kresse, G. & Furthmüller, J. Efficiency of ab-initio total energy calculations for metals and semiconductors using a plane-wave basis set. Comput. Mater. Sci. 6, 15–50 (1996).
2. Kresse, G. & Furthmüller, J. Efficient iterative schemes for ab initio total-energy calculations using a plane-wave basis set. Phys. Rev. B 54, 11169–11186 (1996).
3. Zhang, Y. & Yang, W. Comment on “Generalized gradient approximation made simple”. Phys. Rev. Lett. 80, 890 (1998).
4. Perdew, J. P., Burke, K. & Ernzerhof, M. Generalized gradient approximation made simple. Phys. Rev. Lett. 77, 3865–3868 (1996).
5. Grimme, S., Ehrlich, S. & Goerigk, L. Effect of the damping function in dispersion corrected density functional theory. J. Comput. Chem. 32, 1456–1465 (2011).
6. Gillan, M. J., Alfè, D. & Michaelides, A. Perspective: How good is DFT for water? J. Chem. Phys. 144, 130901 (2016).
7. Morawietz, T. et al. How van der Waals interactions determine the unique properties of water. Proc. Natl Acad. Sci. USA 113, 8368–8373 (2016).
8. Marsalek, O. & Markland, T. E. Quantum dynamics and spectroscopy of ab initio liquid water: the interplay of nuclear and electronic quantum effects. J. Phys. Chem. Lett. 8, 1545–1551 (2017).
9. Perlt, E. et al. Finding the best density functional approximation to describe interaction energies and structures of ionic liquids in molecular dynamics studies. J. Chem. Phys. 148, 193835 (2018).
10. Bella, J., Brodsky, B. & Berman, H. M. Hydration structure of a collagen peptide. Structure 3, 893–906 (1995).
11. Park, Y. et al. Scalable parallel algorithm for graph neural network interatomic potentials in molecular dynamics simulations. J. Chem. Theory Comput. 20, 4857–4868 (2024).
12. Lee, S. Y. et al. FlashTP: fused, sparsity-aware tensor product for machine learning interatomic potentials. Forty-second International Conference on Machine Learning. 267, 33143–33156 (2025).
13. Sun, H. COMPASS: an ab initio force-field optimized for condensed-phase applications overview with details on alkane and benzene compounds. J. Phys. Chem. B 102, 7338–7364 (1998).
14. Akkermans, R. L. C., Spenley, N. A. & Robertson, S. H. COMPASS III: automated fitting

workflows and extension to ionic liquids. Mol. Simul. 47, 540–551 (2021).
15. Thompson, A. P. et al. LAMMPS — a flexible simulation tool for particle-based materials modeling at the atomic, meso, and continuum scales. Comput. Phys. Commun. 271, 108171 (2022).
16. Gowers, R. J. et al. MDAnalysis: a Python package for the rapid analysis of molecular dynamics simulations. Los Alamos National Laboratory Rep. LA-UR-19-29136 (2019).
17. Michaud-Agrawal, N. et al. MDAnalysis: a toolkit for the analysis of molecular dynamics simulations. J. Comput. Chem. 32, 2319–2327 (2011).
18. Stukowski, A. Visualization and analysis of atomistic simulation data with OVITO–the Open Visualization Tool. Model. Simul. Mater. Sci. Eng. 18, 015012 (2010).
19. Murch, G. E. The Haven ratio in fast ionic conductors. Solid State Ionics 7, 177–198 (1982).
20. Nürnberg, P. et al. Superionicity in ionic-liquid-based electrolytes induced by positive ion–ion correlations. J. Am. Chem. Soc. 144, 4657–4666 (2022).
21. Han, J. & Fussenegger, M. Designing supramolecular catalytic systems for mammalian synthetic metabolism. Nat. Rev. Mater. 10, 584–603 (2025).
22. Lu, Y.-N. et al. High ion-conductive hydrogel: soft, elastic, with wide humidity tolerance and long-term stability. ACS Appl. Mater. Interfaces 16, 60992–61003 (2024).
23. Zhao, W. et al. Engineering tough and stretchable ion-conductive hydrogels with hierarchical dynamic bonds for deep learning-assisted gesture recognition. Adv. Funct. Mater. 36, e75831 (2026).
24. Xing, Y. et al. Unlocking ultra-low temperature performance: an anti-freezing, high-conductivity, biodegradable hydrogel electrolyte for supercapacitors down to −60 °C. Chem. Sci. 16, 19253–19262 (2025).
25. Han, F. et al. High-conductivity, self-healing, and adhesive ionic hydrogels for health monitoring and human-machine interactions under extreme cold conditions. Adv. Sci. 12, 2412726 (2025).
26. Liu, J. et al. Polyzwitterionic hydrogel electrolytes via ultrafast autocatalytic gelation process for flexible Zn-ion hybrid supercapacitors. Chem. Eng. J. 483, 149360 (2024).
27. Zhu, J. et al. Double-cross-linking strengthened cellulose nanofibrils/poly(vinyl alcohol) hydrogel electrolyte for all-climate supercapacitors. ACS Appl. Polym. Mater. 7, 14246–14258 (2025).
28. He, P. et al. Moisture self-regulating ionic skins with ultra-long ambient stability for self-healing energy and sensing systems. Nano Energy 128, 109858 (2024).

29. Bi, S. et al. High-density ionic skin via direct microlithography of photosensitive ionogel. Adv. Funct. Mater. 35, 2414138 (2025).
30. He, X. et al. Highly conductive and stretchable nanostructured ionogels for 3D printing capacitive sensors with superior performance. Nat. Commun. 15, 6431 (2024).
31. Jiang, H. et al. Design of COF crosslinker within polymeric ionogels for simultaneous enhancement of toughness and ionic conductivity. Adv. Funct. Mater. 36, 2530871 (2026).
32. Lyu, X. et al. Multi-modal sensing ionogels with tunable mechanical properties and environmental stability for aquatic and atmospheric environments. Adv. Mater. 36, 2410572 (2024).
33. Li, Z. et al. High-performance solid-state ionic conductive elastomers via hard-phase enrichment strategy: synergistic enhancement of mechanical properties and ionic conductivity with sustainable LiTFSI recycling. Adv. Funct. Mater. 35, 2503416 (2025).
34. Sun, L. et al. Elastic and ultra-stable ionic conductors for long-life-time soft robots working at extreme environments. Nat. Commun. 16, 6004 (2025).
35. Li, M. et al. Organic/inorganic hybrid ionogel fiber with synergistically enhanced mechanical and ionic thermoelectric performances. Adv. Funct. Mater. 35, 2415856 (2025).
36. Ye, Y. et al. Ultrastretchable ionogel with extreme environmental resilience through controlled hydration interactions. Adv. Funct. Mater. 33, 2209787 (2023).
37. Li, N. et al. Rapid self-assembly of robust ultrathin ionogel films for high-performance bioelectronics. Sci. Adv. 12, eaeb4391 (2026).
38. Zhao, W. et al. Radiation controllable construction of multifunctional ionogel with a soft-rigid structure for high-performance ionic skin. Cell Rep. Phys. Sci. 5, 102107 (2024).
39. Wu, H. et al. Strong adhesive, high conductive and environmentally stable eutectogel based on “water in deep eutectic solvent”: ultrasensitive flexible temperature and strain sensors. Chem. Eng. J. 497, 154883 (2024).
40. Huang, Y. et al. High strength, strain, and resilience of gold nanoparticle reinforced eutectogels for multifunctional sensors. Adv. Sci. 12, 2416318 (2025).
41. Zhang, H. et al. Strong and tough physical eutectogels regulated by the spatiotemporal expression of non-covalent interactions. Adv. Funct. Mater. 32, 2206305 (2022).
42. Wang, J. et al. Freeze-resistant, conductive, and robust eutectogels of metal salt-based deep eutectic solvents with poly(vinyl alcohol). ACS Appl. Polym. Mater. 4, 2057–2064 (2022).

**Supplementary Video 1. Dynamic trajectory of $[Ch]^+$ ions within the interstitial voids of the collagen matrix.** Dynamic trajectory tracking of a 2×2×2 replicate cell showing that $[Ch]^+$ ions (orange) remain anchored within the interstitial voids between adjacent collagen helices (green and blue) throughout the simulation. This indicates that these confined cations function as stable electrostatic bridges that physically interconnect adjacent collagen molecules.